



École Polytechnique Fédérale de Lausanne Politecnico di Torino

Modeling, validation and optimal design of DC electromagnets for the guidance of high-speed hyperloop vehicles

by Michele Fabbri Master Thesis

Approved by the Examining Committee:

Eng. Lucien Pierrejean Thesis Advisor

Prof. Aldo Canova Thesis Supervisor

Prof. Mario Paolone Thesis Supervisor

cons	La nobiltà dell'uomo, acquistata in cento s nsiste nel farsi signore della materia e nel piega — Primo Levi, Il sistem	rla alla propria volontà.	
D	Dedicato a mia nonna Franca Pellegrinetti.		

Acknowledgments

Firstly, I would like to express my gratitude to my thesis supervisors, Prof. Mario Paolone (EPFL) and Prof. Aldo Canova (PoliTo), for their invaluable guidance, encouragement, and patience throughout the development of this work.

Secondly, but no less importantly, I want to thank my thesis advisor, Lucien Pierrejean. It has truly been a pleasure to work alongside you. I have grown immensely by following your work ethic, dedication, and methodological as well as technical advice. You taught me what it means to be an engineer. *Merci beaucoup, Lucien!*

I am also grateful to my colleagues at the DESL for their stimulating discussions, technical support, and for creating such a welcoming research environment. In particular, a special thank you goes to Simone Rametti.

I wish to dedicate a sincere thank you to my lifelong friends, whose support, energy, passion, and irony helped me face the challenges of both high school and university. Thanks to Lorenzo, Manuel, Giacomo, Andrea (Cipro), Matilde, Sofia, and Federico. I will surely bring you a "popone" to celebrate.

I would also like to acknowledge my colleagues and friends from the University of Pisa, with whom I shared the years of my Bachelor's degree. The discussions and advice we exchanged, both technical and existential, were invaluable for my professional and personal growth. So, thank you, Francesco, Arianna, Lisa, Alessia, Elia, and Giacomo. I sincerely hope our friendship will last well beyond the university years.

When I moved to Turin, I had the pleasure of meeting a friend with whom I shared thoughts and projects over the last two years. Thank you, Lorenzo, for your academic passion and broad knowledge, which have deeply influenced me.

Finally, but only for chronological order, I want to thank Anna. Even though we have known each other for only seven months, it feels as if I have always known you. Thank you for being by my side and encouraging me, even across the distance.

Last but certainly not least, I want to thank my family for allowing me to live and enjoy this beautiful journey.

Lausanne, September 4, 2025

Michele Fabbri

Abstract

This thesis develops a complete workflow for the modeling, validation, and optimal design of DC electromagnets intended for magnetic levitation in high-speed Hyperloop vehicles. An analytical model was first established for stationary conditions and validated against finite element method (FEM) simulations, enabling the development of an optimization environment to maximize levitation force under physical and geometrical constraints. The study was then extended to dynamic conditions, evaluating both the reduction in levitation force and the generation of drag force. Two FEM approaches, the Lorentz Term and the Moving Mesh, were compared, and the analytical model was validated against their results, confirming its reliability for rapid design iterations. Finally, the workflow was applied to a real-world Hyperloop prototype at EPFL, where electromagnets were benchmarked against mechanical wheels. The study demonstrated that electromagnets can provide competitive results, with the additional advantage of enabling full vehicle levitation. The contributions of this work include an optimization framework for electromagnet design under stationary conditions, an extended analytical model for dynamic conditions, a comparative analysis of FEM approaches, and an application to a practical Hyperloop case study. The proposed methodology provides tools of both methodological and practical value, extendable beyond Hyperloop to a wide range of electromagnetic devices.

List of symbols

LCA - Life Cycle Assessment

WTW - Well to Wheel

EDS - Electrodynamic Suspension

EMS - Electromagnetic Suspension

LIM - Linear Induction Motor

 $l\ [\mathrm{m}]$ - Electromagnet's length

h [m] - Electromagnet's height

w [m] - Electromagnet's width

 μ [H/m] - Magnetic permeability

 $\rho \; [\Omega \cdot m]$ - Electric resistivity

 ϵ [F/m] - Electric permittivity

 $\mathcal{R}[H^{-1}]$ - Magnetic reluctance

 $S [m^2]$ - Yoke's cross section

MMF $[A \cdot t]$ - Magnetomotive Force

 δ [m] - Air gap width

N - Coil's number of turns

 $A \text{ [mm}^2\text{]}$ - Wire's cross section

J [A/mm²] - Current density

w [m] - Tooth width

 ξ [W/N] - Losses-force factor

 Σ - Fringing factor

 σ_x - Fringing factor in x-direction

 σ_{v} - Fringing factor in y-direction

FEM - Finite Element Method

e - Relative error

 P_I [W] - Joule losses

v [m/s] - Displacement velocity

List of figures

- 1.1 LCA and WTW emission factors for different means of transportation
- 1.2 Representation of the EMS system and the EDS system
- 1.3 EPFLoop pod
- 2.1 Application of Gauss's law for magnetism to the yoke
- 2.2 Application of Ampère-Maxwell's law to the yoke
- 2.3 Electromagnet's geometry and dimensions
- 2.4 2D section of the electromagnet and the rail, in red the fringing fluxes
- 2.5 General geometry for Schwarz-Christoffel mapping
- $2.6\ Schwarz\text{-}Christoffel$ mapping on the tooth geometry, in red a fringing flux line
- 2.7 Construction of the total air gap reluctance
- 2.8 Geometry used to compute the fringing factors
- 3.1 Geometry of the 2D COMSOL model
- 3.2 Magnetic flux density distribution $\|\vec{B}\|$ in the 2D COMSOL simulation
- 3.3 Geometry of the 3D COMSOL model
- 3.4 Magnetic flux density distribution $\|\vec{B}\|$ in the 3D COMSOL simulation
- 3.5 Mesh convergence study: levitation force F_{lev} as a function of element size
- 3.6 Force changing the air gap width: simple reluctance model vs. 2D FEM
- 3.7 Force changing the air gap width: Schwarz-Christoffel correction vs. 2D FEM
- 3.8 Comparison between the force generated by the analytical models and the 3D simulations
- 3.9 Effect of length *l* on specific force and losses-to-force ratio
- 3.10 Effect of tooth width w on specific force and losses-to-force ratio
- 3.11 Effect of current density *J* on specific force and losses-to-force ratio
- 4.1 Pareto front
- 4.2 Optimal decision variables
- 4.2 Optimal electromagnet's parameters
- 5.1 Geometry transformation to simplify the analytical derivation
- 5.2 Integration paths for Ampère's law. Left: xy-plane. Right: zy-plane
- 5.3 Residue theorem integration paths
- 6.1 Electromagnet orientations with respect to the direction of motion: parallel and perpendicular
- 6.2 Half of the electromagnet geometry used in the simulations. The PMC boundary condition enforces the correct symmetry

- 6.3 Relative magnetic permeability distribution in the rail, used to validate mesh adequacy
- 6.4 Detail of the mesh used for Lorentz Term simulations
- 6.5 Detail of the mesh used for Moving Mesh simulations
- 6.6 Magnetic flux density in a plane intersecting the middle of the electromagnet for the Lorentz Term simulation
- 6.7 Magnetic flux density in a plane intersecting the middle of the electromagnet for the Moving Mesh simulation at steady state
- 6.8 Levitation force and drag force computed with the Moving Mesh and Lorentz Term features at a velocity of 16 m/s
- 6.9 Comparison between the magnitudes of the air gap magnetic flux densities with the Moving Mesh and the Lorentz Term
- 6.10 Comparison of levitation forces (left plot) and drag forces (right plot) computed with the Lorentz Term and the analytical model

List of tables

- 3.1 Electromagnet parameters for model comparison
- 3.3 Mesh parameters for different refinement levels
- 3.11 Effect of current density *J* on specific force and losses-to-force ratio
- 3.4 Summary of validation results for air gap variation
- 4.1 Decision variables
- 4.2 Optimal electromagnet's parameters
- 6.1 Electromagnet parameters used for feature comparison
- 6.2 Computation times for the Lorentz Term and Moving Mesh simulations at $v = 16 \,\mathrm{m/s}$
- $6.3\,Comparison$ between electromagnets and wheels for pod levitation at 16m/s

Contents

Ac	Acknowledgments		1	
Ał	ostra	ct		2
1	Intr	oducti	on	10
	1.1	Conte	ext	10
	1.2	Motiv	ration of the research	12
		1.2.1	Real-world case study	13
2	Ana	lytical	model in stationary conditions	14
	2.1	Motiv	ration and model definition	14
		2.1.1	Maxwell's equations	15
		2.1.2	Model hypotheses	16
		2.1.3	Hopkinson's laws	16
		2.1.4	Force evaluation	18
		2.1.5	Specific force	19
		2.1.6	Losses	21
	2.2	Abser	nce of fringing flux hypothesis compensation	22
		2.2.1	Empirical fringing factors	23
	2.3	Schw	arz-Christoffel conformal mapping	24
		2.3.1	Derivation of the air gap reluctance	25
		2.3.2	Reluctance calculation	28
		2.3.3	Application of the Schwarz-Christoffel transformation to the electromagnet $$. $$.	29
	2.4	Infini	te magnetic permeability hypothesis compensation	31
	2.5	Concl	luding remarks	32
3	2D :	and 3D	simulations in static conditions	33
	3.1	COM	SOL models	34
		3.1.1	Definition of the problem	34
		3.1.2	2D COMSOL model	35
		3.1.3	3D COMSOL model	36
		3.1.4	Materials	37

		3.1.5 Mesh convergence study	37
	3.2	Simulation results	39
		3.2.1 Error metric	39
		3.2.2 Comparison between the 2D analytical and COMSOL models	39
		3.2.3 Comparison between the 3D analytical and COMSOL models	41
	3.3	Comparison varying other dimensions	42
		3.3.1 Variation in length l	42
		3.3.2 Variation in tooth width w	43
		3.3.3 Variation in current density J	43
	3.4	Conclusion remarks and practical implications	44
		3.4.1 Key observations	44
		3.4.2 Computational efficiency	44
		3.4.3 Recommended modeling workflow	45
4	Con	ometry optimization	46
7	4.1	· -	46
	4.2	Design optimization	
	4.3	Optimal design	
	4.5	4.3.1 Real-world application	
	4.4	Flexibility of the Optimization Problem	
	1.1	4.4.1 Concluding remarks	
		inii Goneraanig remarke	50
5	Ana		54
	5.1	Introduction	
	5.2	Analytical model's derivation	
		5.2.1 Model' hypotheses and starting equations	
		5.2.2 Derivation of the total air gap flux density	
		5.2.3 Levitation force calculation	
		5.2.4 Drag force calculation	
	5.3	Concluding remarks	68
6	2D a	and 3D simulations in dynamic conditions	69
	6.1	Definition of the problem	71
		6.1.1 Lorentz Term	71
		6.1.2 Moving Mesh	72
		6.1.3 Materials	73
		6.1.4 Exploitation of symmetries	74
		6.1.5 Selection of the mesh	75
	6.2	3D simulations	76
	0.2	ob diffututions	
	0.2		77
	0.2	6.2.1 Lorentz Term	77 77

Bibliography					
7	Con	clusion	83		
	6.5	Concluding remarks	82		
	6.4	Real-world case study	81		
	6.3	Analytical model and simulations	80		

Chapter 1

Introduction

1.1 Context

The transportation sector is one of the largest contributors to global CO_2 emissions, accounting for approximately 20% of total global emissions [1]. Road transport is responsible for approximately three-quarters of this, while aviation and rail contribute about 12% and 1%, respectively, corresponding to a combined 3% of global CO_2 emissions. Reducing transportation-related emissions requires the development and implementation of several solutions, depending on the travel range. For urban transportation, there is a pressing need to transition toward more sustainable options [2]. For short to medium range travel, rail transport is generally the most environmentally friendly option, as it produces the lowest emissions per passenger-kilometer [3].

Figure 1.1 presents the Life Cycle Assessment (LCA) and Well-to-Wheel (WTW) emission factors, expressed in grams of CO_2 per passenger-kilometer, for different means of transportation.

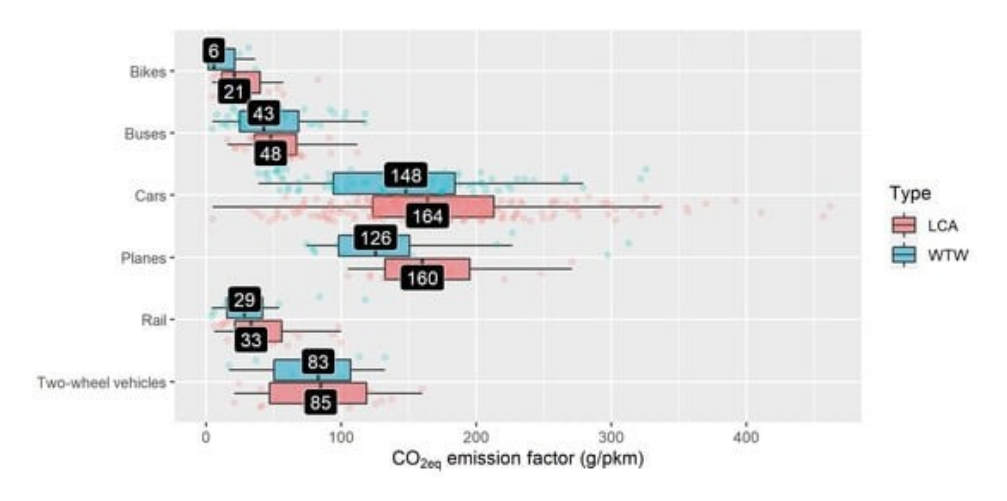


Figure 1.1: LCA and WTW emission factors for different means of transportation

However, for long-distance travel, rail is often considered too slow, leading to a preference for airplanes, which are significantly more polluting.

In this context, a new transportation concept, the Hyperloop, has appeared as a potential mode to mitigate the high emissions associated with air travel, while maintaining its cruising speed. The Hyperloop is a magnetic levitation (MagLev) train operating inside a depressurized tube, reducing aerodynamic drag. This configuration enables low energy losses and drag, allowing speeds comparable to those of an airplane with significantly lower emissions (approximately $10 \, \mathrm{g} \, CO_2/\mathrm{pkm} \, [4]$). The idea of a train traveling through a depressurized tube was first proposed by Robert Goddard in the early 20th century. Feasibility studies were later conducted in the 1970s under the Swissmetro project. However, despite promising results, the technology available at the time was insufficient to reduce costs and losses to levels competitive with already established transport systems.

Today, advances in battery technology, power electronics, and efficiency in electrical components have revived interest in making the Hyperloop a viable transportation solution.

Various levitation systems have been proposed [5], including:

- Air bearings, where levitation is achieved via pressurized air;
- Electrodynamic suspension (EDS), which uses permanent magnets (often in Halbach array configurations) to generate lift through relative motion over a conductive rail;
- Electromagnetic suspension (EMS), where electromagnets interact with a ferromagnetic rail to produce an attractive force. Placing the magnets underneath the rail allows for this attraction to result in levitation. Alternatively, there is the possibility of placing the magnets above the train to achieve the same result.

A visual comparison of the EMS and EDS systems is shown in Fig. 1.2.

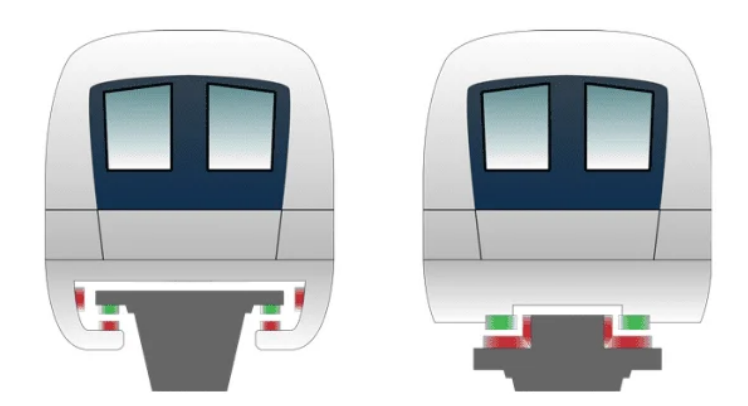


Figure 1.2: Representation of the EMS system (left) and the EDS system (right) [6]

Hyperloop propulsion can be provided by a linear electric motor, a linear induction motor (LIM), or a homopolar linear synchronous motor (H-LSM) [7].

1.2 Motivation of the research

The purpose of this thesis is to develop a systematic workflow for the design and performance assessment of electromagnets used in magnetic levitation systems, dealing with both stationary and dynamic operating conditions. A particular focus is placed on the phenomenon of electromagnetic drag, which is still not sufficiently characterized in the current literature. This work aims to investigate drag generation in detail, combining analytical modeling with FEM simulations. The thesis is structured as follows:

- 1. Development of an analytical model in stationary conditions, used for design optimization to maximize the levitation force under given geometrical and physical constraints.
- 2. Validation of the analytical model through comparison with high-fidelity FEM simulations to assess its accuracy and limitations.
- 3. Definition of an optimization environment tailored to electromagnet design.
- 4. Extension of the analytical framework to dynamic conditions, allowing the evaluation of both the reduction in levitation force and the generation of drag force during motion.
- 5. Validation of the dynamic analytical model through numerical simulations in COMSOL [8].

The contribution of this thesis to the scientific literature is threefold:

- the development of a general optimization workflow applicable to the design of electromagnets and, more generally, to electric machines;
- the formulation of an analytical model capable of predicting both the decrease in levitation force and the emergence of drag force under dynamic conditions;
- the implementation of a coherent simulation environment in COMSOL, useful as a benchmark for the validation of analytical results.

Beyond academic contributions, the results of this thesis have practical relevance for the development of advanced transportation systems, such as magnetic levitation trains and Hyperloop technologies, where efficiency and reliability are critical. By providing accurate tools to predict and optimize both levitation and drag forces, the proposed workflow supports the design of more energy-efficient and cost-effective electromagnets. Furthermore, the methodologies developed here can be readily extended to a broader class of electric machines, thereby contributing to the improvement of sustainable and high-performance electromagnetic technologies.

1.2.1 Real-world case study

This study is part of a research project conducted by the Distributed Energy Systems Laboratory (DESL) at EPFL.

The main objective of the project is to design and develop a scaled prototype of a Hyperloop system to evaluate the feasibility of implementing this technology in large-scale infrastructures.

The pod, whose initial prototype is shown in Fig. 1.3, is conceived as an energy-autonomous vehicle. The batteries mounted on the chassis supply the energy required to propel the pod using energy-optimized linear induction motors (LIMs). One of the major challenges with this solution lies in the low energy density of batteries, typically a few hundred Wh/kg, which results in limited autonomy. Consequently, every component of the pod must be carefully optimized for maximum energy efficiency.

Since it is not feasible to construct an infinitely long test track, the pod was tested on a circular track. This decision introduced additional challenges, in particular, the need to counteract the centrifugal force generated during motion. To address this, mechanical wheels were employed, which oppose a force of approximately 1000N and generate around 250W of frictional losses.

In this context, the use of electromagnets rather than wheels for the guidance system, specifically, the components responsible for counterbalancing the centrifugal force during turns, was investigated. The ultimate goal was to develop a fully levitating vehicle while minimizing the energy consumption of the electromagnets, even at high velocities. From the space available in the pod, two electromagnets were selected to improve the controllability of the system. Their maximum dimensions were constrained to $l \times h \times b = 350 \times 50 \times 50$ mm.

The research presented in this thesis directly addresses this challenge by proposing analytical models and simulation tools capable of predicting and optimizing the performance of such electromagnets under both stationary and dynamic operating conditions.



Figure 1.3: EPFLoop pod

Chapter 2

Analytical model in stationary conditions

2.1 Motivation and model definition

The analytical model in stationary conditions is fundamental for guiding the design of a stationary electromagnet to maximize the generated levitation force while respecting given geometrical and physical constraints. In this context, the analytical model will serve as the basis for an optimization problem, in which the optimal parameter values will be determined in a deterministic manner. Several modeling approaches can be applied to electromagnetic actuators, such as the levitation device studied in this work. Some approaches rely directly on the solution of Maxwell's equations, for example, by calculating the electromagnetic field in the air gap through coordinate transformations. Other approaches simplify the general field equations by representing, under certain assumptions, the device as a magnetic equivalent circuit.

The latter approach, although generally considered less accurate due to the simplifications involved, offers significant advantages: it is computationally lighter, easier to implement analytically, and, if properly parametrized, can produce results comparable to those obtained by solving the full Maxwell's equations.

On the basis of these considerations, the magnetic equivalent circuit method was selected for the initial stage of this study.

To improve the accuracy of the model, the Schwarz-Christoffel conformal mapping technique [9] is later applied to account for the effects of the fringing flux and to better approximate the distribution of magnetic flux density in the air gap.

Finally, the results obtained from the analytical model are compared with finite element simulation data to evaluate its accuracy and to assess its suitability for design optimization.

2.1.1 Maxwell's equations

For completeness, Maxwell's equations in their general form are recalled below:

$$\vec{\nabla} \cdot \vec{D} = q$$
 (Gauss's law for the electric field) (2.1)

$$\vec{\nabla} \cdot \vec{B} = 0$$
 (Gauss's law for magnetism) (2.2)

$$\vec{\nabla} \times \vec{E} = -\frac{\partial \vec{B}}{\partial t}$$
 (Faraday's law) (2.3)

$$\vec{\nabla} \times \vec{H} = \vec{J} + \frac{\partial \vec{D}}{\partial t}$$
 (Ampère–Maxwell law) (2.4)

The constitutive relations are:

$$\vec{B} = \mu \vec{H}, \quad \vec{E} = \rho \vec{D}, \quad \vec{D} = \epsilon \vec{E}$$

where μ is the magnetic permeability, ρ the electric resistivity, and ϵ the electric permittivity of the medium.

A direct consequence of these equations is that changes in the electromagnetic fields propagate at a finite speed, determined by the properties of the medium, which causes a delay between the variation of the sources and the resulting fields.

However, when the characteristic dimensions of the device are much smaller than the wavelength associated with the time variation of the fields, and variations are slow, the quasi-static approximation can be applied. In this approximation, the system is treated as if it were in steady state at each instant, greatly simplifying the analysis.

Under these conditions, the equations reduce to:

$$\vec{\nabla} \cdot \vec{D} = q \tag{2.5}$$

$$\vec{\nabla} \cdot \vec{B} = 0 \tag{2.6}$$

$$\vec{\nabla} \times \vec{E} = -\frac{\partial \vec{B}}{\partial t} \tag{2.7}$$

$$\vec{\nabla} \times \vec{H} = \vec{J} \tag{2.8}$$

Here, Eq.(2.6) enforces magnetic flux conservation (absence of magnetic monopoles), and Eq.(2.8) relates the magnetic field circulation to the total current, forming the basis for the magnetic circuit approach used in this work.

2.1.2 Model hypotheses

Under the following assumptions, Eqs. (2.6) and (2.8) can be applied in their integral form to develop the magnetic circuit model:

- 1. Linear, homogeneous, and isotropic materials.
- 2. Iron with high magnetic permeability: $\mu_{fe} \rightarrow \infty$.
- 3. Negligible magnetic flux fringing.
- 4. Iron with zero electrical conductivity and a hysteresis cycle of zero area.

The first assumption ensures that the electromagnetic fields are uniformly distributed in the cross-section of the yoke and remain orthogonal to that section.

The second assumption implies that the magnetic field is almost entirely confined within the yoke, allowing leakage flux in the surrounding air to be neglected.

The third assumption completes the second, ensuring that the flux remains confined and orthogonal to the cross-section also in the air gap region.

Finally, the fourth assumption means that iron losses, due to eddy currents or hysteresis, can be neglected.

These idealizations make the model analytically tractable, while still providing accurate estimates for preliminary design calculations. More refined models can later relax some of these assumptions if higher accuracy is required.

2.1.3 Hopkinson's laws

Hopkinson's laws are the primary tools used to analyze magnetic devices; for clarity, they can be considered as the magnetic equivalent of Kirchhoff's laws for electrical circuits.

First Hopkinson's law.

It can be derived directly from Gauss's law for magnetism (Eq. 2.6) in its integral form:

$$\oint_{sup} \vec{B} \, d\vec{s} = 0 \tag{2.9}$$

Consider a closed surface intersecting two or more branches of the yoke (as illustrated in Fig. 2.1). Under the first and second modeling hypotheses, the magnetic flux is orthogonal to the cross-section and entirely confined in the yoke. The integral can therefore be discretized into a summation of

fluxes:

$$\sum_{k=1}^{n} \pm \phi_k = 0 \tag{2.10}$$

This expression is the analog of Kirchhoff's first law (current law), with magnetic flux ϕ playing the role of electric current.

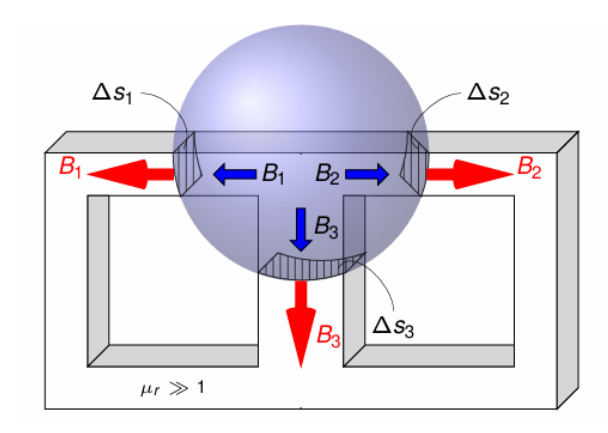


Figure 2.1: Application of Gauss's law for magnetism to the yoke [10]

Second Hopkinson's law.

This law follows from the Ampère-Maxwell equation (Eq. 2.8) in its integral form:

$$\oint_{\vec{l}} \vec{H} \, d\vec{l} = \int_{sup} \vec{J} \, d\vec{s} \tag{2.11}$$

In the geometry shown in Fig. 2.2, and under the first hypothesis, the magnetic field \vec{H} is always parallel to the path element $d\vec{l}$. The left-hand side of Eq.(2.11) can thus be expressed as a sum of scalar terms, while the right-hand side corresponds to the total current linkage $N \cdot I$.

For a system satisfying the earlier hypotheses, Eq. (2.11) becomes:

$$\sum_{k=1}^{n} \pm H_k l_k = \sum_{h=1}^{m} \pm N_h I_h \tag{2.12}$$

where $N_h I_h$ is the magnetomotive force (MMF) produced by the h-th coil. Using $B = \mu_0 \mu_r H$ and $\phi = B \cdot S$, the above equation can be rewritten as:

$$\sum_{k=1}^{n} \pm \mathcal{R}_k \phi_k = \sum_{h=1}^{m} \pm N_h I_h$$
 (2.13)

with the reluctance of the k-th branch given by:

$$\mathcal{R}_k = \frac{l_k}{\mu_0 \mu_r S_k} \tag{2.14}$$

Here, μ_0 is the permeability of free space, μ_r is the relative permeability of the material, and S_k is the cross-sectional area of branch k.

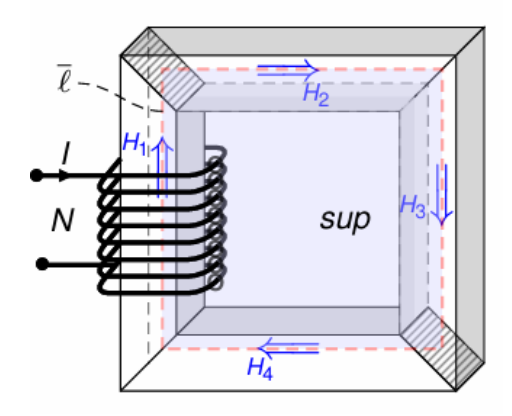


Figure 2.2: Application of Ampère–Maxwell's law to the yoke [10]

In analogy with electric circuits:

- Reluctance \mathcal{R} plays the role of resistance R.
- Magnetic flux ϕ corresponds to electric current I.
- Magnetomotive force (MMF) corresponds to voltage V.

This analogy enables the use of well-established circuit-analysis techniques for magnetic systems.

2.1.4 Force evaluation

The magnetic circuit model determines the magnetic flux in each branch of the electromagnet for a given excitation current. However, the design objective here is not only the computation of the flux distribution in the yoke, but also the evaluation of the attraction force generated between the electromagnet and the rail.

Several methods exist for evaluating electromagnetic forces, including:

- · Maxwell's stress tensor,
- the principle of virtual work,

• and the energy (or coenergy) method.

In this work, the energy method is chosen because it is straightforward to apply in a lumped-parameter model and directly relates inductance variations to force production.

The general expression for the force based on magnetic coenergy is [11]:

$$F = \frac{\partial W'}{\partial x} \bigg|_{i} \tag{2.15}$$

where W' is the magnetic coenergy, x is the position variable, and the derivative is taken at constant current i.

For linear magnetic materials, the coenergy is:

$$W' = \frac{1}{2}L(x)I^2 \tag{2.16}$$

where L(x) is the total inductance, which depends on the geometry (and thus on x). Substituting into the force formula yields:

$$F = \frac{1}{2}I^2 \frac{dL(x)}{dx} \tag{2.17}$$

The inductance can be expressed in terms of the number of turns and total reluctance:

$$L = \frac{\Phi}{I} = \frac{N\phi}{I} = \frac{N^2}{\mathcal{R}_{\text{Tot}}}$$
 (2.18)

where \mathcal{R}_{Tot} is the total reluctance of the magnetic circuit.

In the present case, this is the sum of the reluctances of the yoke, the rail, and the two air gaps.

In more complex topologies, \mathcal{R}_{Tot} must be computed by combining series and parallel reluctances according to the magnetic circuit layout.

Since the only mechanical degree of freedom in the system is the variation of the air gap width, L(x) changes exclusively as a function of the gap size. This dependence allows a direct link between geometry and generated force, which is critical for optimization in the later design stages.

2.1.5 Specific force

The force equations derived above can be applied to a practical case study, following the notation in Fig.2.3.

To simplify calculations, the iron is first assumed to have infinite magnetic permeability ($\mu_{fe} \to \infty$). Under this assumption:

• the reluctance of the iron parts is negligible,

- the magnetic circuit consists only of the two air gap reluctances,
- the magnetomotive force is entirely produced by the coil.

From the simplified magnetic circuit, the total flux is:

$$\phi = \frac{NI}{\mathcal{R}_{\text{tot}}} = NI \frac{\mu_0 l w}{2\delta} = NA \frac{\mu_0 l w}{2\delta} J$$
 (2.19)

where l is the electromagnet length, w the tooth width, δ the air gap width, J the current density, and A the conductor cross-sectional area.

The magnetic flux density in the air gap is:

$$B = \frac{\phi}{S} = \frac{\phi}{lw} = \frac{\mu_0 NI}{2\delta} = \frac{\mu_0 NAJ}{2\delta}$$
 (2.20)

From this, the force is:

$$F = \frac{B^2 S}{\mu_0} = \mu_0 \frac{N^2 I^2}{4\delta^2} l w = \mu_0 \frac{N^2 A^2 J^2}{4\delta^2} l w$$
 (2.21)

The equation above shows that F increases with the total conductor cross-section $N \cdot A$, the current density J, and the transverse section $l \cdot w$, and decreases with the square of the air gap width δ .

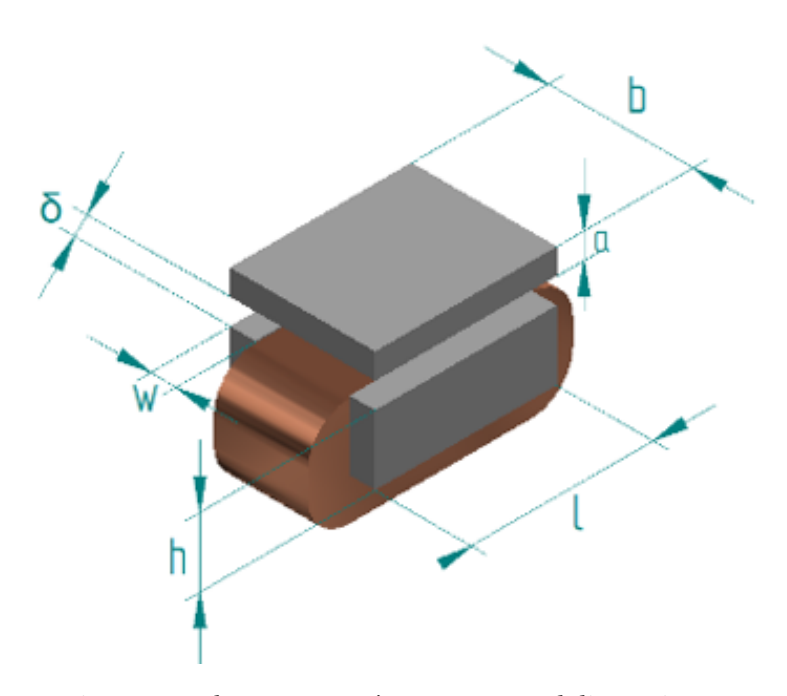


Figure 2.3: Electromagnet's geometry and dimensions

A more useful metric for lightweight design is the specific force, i.e. the ratio between generated force and total device mass:

$$f = \frac{F}{m} = \frac{\mu_0 N^2 A^2 J^2}{4\delta^2} \frac{lw}{\rho_{fe} [lw(2h+b-2w)] + \rho_{cu} [NA \cdot 2(l+w+\pi(h-w)/2)]}$$
(2.22)

where ρ_{fe} and ρ_{cu} are the densities of iron and copper, respectively. The mass expression follows from straightforward volume × density calculations for the yoke and coils.

Maximizing f is essential for levitation pods, as weight reduction directly improves the performance. If the coil slots are fully packed with conductors, $N \cdot A$ can be replaced by the available slot area (b-2w)(h-w), giving:

$$F = \mu_0 \frac{(b - 2w)^2 (h - w)^2 J^2}{4\delta^2} lw$$
 (2.23)

$$f = \frac{\mu_0 J^2}{4\delta^2} \frac{lw(b-2w)^2 (h-w)^2}{\rho_{fe} [lw(2h+b-2w)] + \rho_{cu} [(b-2w)(h-w) \cdot 2(l+h)]}$$
(2.24)

These compact expressions directly link geometry and current density to both the total force and the specific force, making them particularly useful for a preliminary optimization study.

2.1.6 Losses

If the iron core is assumed to be non-conductive and the analysis is magnetostatic, the only generated losses are thermal losses in the windings caused by the Joule effect.

In reality, iron has finite electrical conductivity. If the magnetic flux varies with time (e.g., due to relative motion between the electromagnet and rail), eddy currents are induced in the rail, generating additional Joule losses. These are neglected in the present stationary model but are relevant in dynamic operation.

For the electromagnet geometry in Fig. 2.3, the winding resistance is:

$$R = \frac{\rho N \cdot 2\left(l + w + \frac{\pi(h - w)}{2}\right)}{A} \tag{2.25}$$

where ρ is the electrical resistivity of the conductor, N the number of turns, A the conductor cross-sectional area, l, w, h were previously defined. The Joule losses are:

$$P_J = RI^2 (2.26)$$

To assess design efficiency, a losses-to-force factor is defined:

$$\xi = \frac{P_J}{F} \tag{2.27}$$

which represents the power dissipated per unit of generated force. Substituting the expressions for *R* and *F* yields:

$$\xi = \frac{\rho N \cdot 2 (l + w + h_c)}{A} I^2 \cdot \frac{4\delta^2}{\mu_0 N^2 I^2 \cdot lw} = \frac{8\rho \delta^2 (l + w + h_c)}{\mu_0 AN lw}$$
(2.28)

where h_c is the coil height.

A smaller ξ indicates a more efficient design, making this factor useful in early-stage optimization when there is the need to balance force generation and thermal constraints.

2.2 Absence of fringing flux hypothesis compensation

The limitation of the previous model lies in the assumption that the magnetic flux density is always orthogonal to the air gap between the electromagnet and the rail. In reality, this is not the case, especially near the edges of the tooth, where some magnetic flux lines diverge and spread out. This phenomenon is known as fringing, and it is illustrated in Fig. 2.4. To improve the accuracy of the previously introduced simple model, it is essential to account for the effects of fringing fluxes. Fringing causes the effective cross-sectional area of the air gap to increase, reducing the overall magnetic reluctance.

To incorporate this effect into the model, the air gap area is adjusted by applying a fringing factor, which can be determined either empirically or through analytical expressions.

Following this statement, the new reluctance writes:

$$\mathscr{R} = \frac{\delta}{\mu_0 \cdot \Sigma \cdot S} \tag{2.29}$$

Where Σ is the fringing factor.

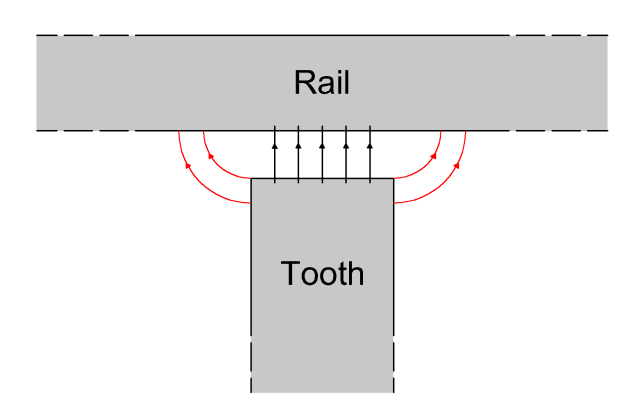


Figure 2.4: 2D section of the electromagnet and the rail, in red the fringing fluxes

2.2.1 Empirical fringing factors

A straightforward approach to computing the air gap reluctance, while accounting for fringing flux, is to apply empirical correction factors. Although these factors can perform well under certain conditions, they remain empirical in nature and may introduce errors into the reluctance formulation. Therefore, they will be presented here for the reader's interest, but they will not be implemented in the analytical model, which instead relies on a formulation based on the Schwarz–Christoffel conformal mapping to account for the effects of fringing flux.

Several empirical formulations have been proposed in the literature. Some of the most commonly used are presented below.

All of them rely on the assumption that the air gap width is much smaller than any of the other dimensions of the electromagnet.

The first correction presented is the McLyman factor [12]:

$$\Sigma = 1 + \frac{\delta}{\sqrt{S}} \ln \frac{2 \cdot l_{window}}{\delta}$$
 (2.30)

Where δ is the air gap width, S is the cross-sectional area of the yoke, and l_{window} is the internal length of the window.

An alternative method, proposed by Kazimierczuk [13], adjusts the effective area based on air gap geometry:

$$\Sigma = 1 + \frac{\delta \cdot (l + w + 2\delta)}{l \cdot w} \tag{2.31}$$

Where w and l are the lengths of the two sides of the iron yoke.

A further approximation by Hurley and Wölfe [14] writes:

$$\Sigma = \frac{(w+\delta)(l+\delta)}{l \cdot w} \tag{2.32}$$

The fringing factors must then be substituted in Eq. (2.29) to provide a more accurate estimation of the air gap reluctance.

However, a limitation of these empirical formulas lies in their nature: they are approximations derived from simplified assumptions and experimental observations. As such, they do not fully account for the specific geometry of the actual electromagnet, which may lead to discrepancies between the analytical model and the real electromagnetic force. However, employing these empirical corrections provides a better approximation than relying only on the basic reluctance model, which entirely neglects the influence of fringing.

For the scope of this study, the empirical fringing factors will not be employed, as a model with an analytical derivation, which considers the geometry of the electromagnet, will be preferred.

For this reason, the Schwarz-Christoffel conformal mapping was used to derive a value of the air gap reluctance that takes into account the presence of the fringing fluxes.

2.3 Schwarz-Christoffel conformal mapping

The Schwarz-Christoffel conformal mapping, as introduced previously, is a mathematical tool used to transform complex geometries into simpler ones. By applying this technique, fringing flux lines are mapped into straight lines, allowing for a straightforward evaluation of the magnetic reluctance. Unlike empirical fringing factors, this method can be used regardless of the geometry and provides accurate results when compared to the simulations (Chapter 3).

In practice, as shown in Fig. 2.6, the derivation proceeds in two steps. First, the geometry of the tooth is simplified by mapping it onto the upper half-plane, with each vertex corresponding to a specific point on the boundary. Then, a second conformal transformation maps this half-plane onto a strip, bounded by two parallel lines. In this transformed domain, the magnetic flux lines become orthogonal to the yoke's cross-section, allowing the reluctance to be computed using the basic expression given in Eq.(2.14).

The following derivation is based on [9], [15] and [16].

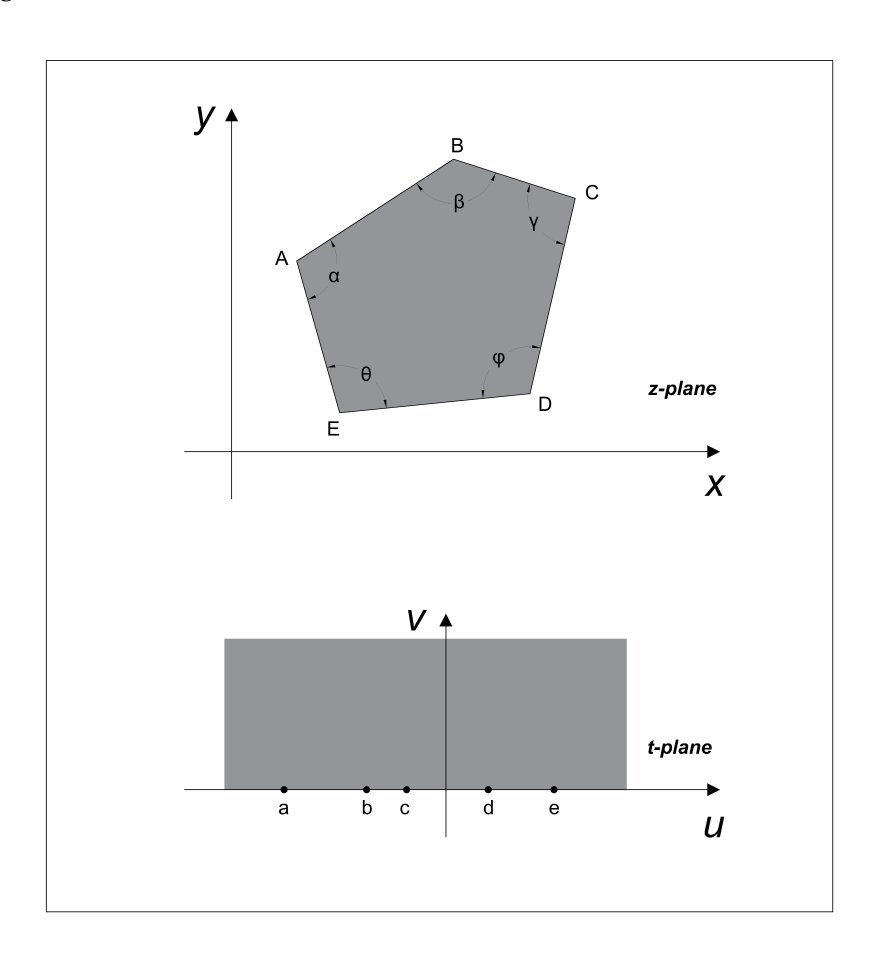


Figure 2.5: General geometry for Schwarz-Christoffel mapping

In complex analysis, a conformal map is a transformation between two subsets \mathbb{R}^n , which preserves angles but not necessarily lengths.

To give a formal mathematical definition, a function of the type

$$w = q(t) = u(x, y) + i v(x, y)$$
(2.33)

That defines a complex variable w = u + jv as a function of the variable t = x + jy is called conformal if it preserves angles. In particular, as already explained, the Schwarz-Christoffel mapping is a useful tool for simplifying the geometry of a closed or semi-closed polygon. It consists of a conformal map of the upper half-plane onto the interior of a polygon. Its existence is indeed guaranteed by the Riemann mapping theorem.

Considering the polygon depicted in Fig. 2.5, the Schwarz-Christoffel transformation from the real axis of the t-plane to the interior boundaries of the polygon in the z-plane is given by the solution of the following differential equation:

$$\frac{dz}{dt} = \frac{K}{(t-a)^{1-(\alpha/\pi)}(t-b)^{1-(\beta/\pi)}(t-c)^{1-(\gamma/\pi)}(t-d)^{1-(\phi/\pi)}(t-e)^{1-(\theta/\pi)}}$$
(2.34)

Where *K* is a constant, *a*, *b*, *c*, *d*, *e* are the points on the real axis of the t-plane, corresponding to the vertices of the polygon in the z-plane, and α , β , γ , φ , θ are the interior angles of the vertices of the polygon in the z-plane.

2.3.1 Derivation of the air gap reluctance

Solving the Schwarz-Christoffel differential equation and considering the boundary conditions leads to the transformation equation.

In the following computations, a first Schwarz-Christoffel mapping will be applied to simplify the geometry of the air-gap region. Subsequently, a second mapping will be used to reconstruct a new geometry that facilitates the computation of the air-gap reluctance.

From the t-plane to the z-plane

The first transformation is performed to map the geometry of the teeth from the t-plane to the z-plane. Considering Fig. 2.6, the Schwarz-Christoffel differential equation takes the following form:

$$\frac{dz}{dt} = \frac{K}{t(t-1)^{-\frac{1}{2}}} = K \frac{\sqrt{t-1}}{t}$$
 (2.35)

Where, in the t-plane, point 1 lies in the origin (a = 0) and has a zero angle $(\alpha = 0)$. While point 2, instead, lies in b = 1 and has an angle of $\beta = \frac{3\pi}{2}$.

The solution to the previous differential equation is the following:

$$z(t) = -jK_1(2\ln(1+\sqrt{1-t}) - \ln(t) - 2\sqrt{1-t}) + C_1$$
(2.36)

Where K_1 and C_1 are respectively the Schwarz-Christoffel and the integration constants that need to be determined by imposing the boundary conditions.

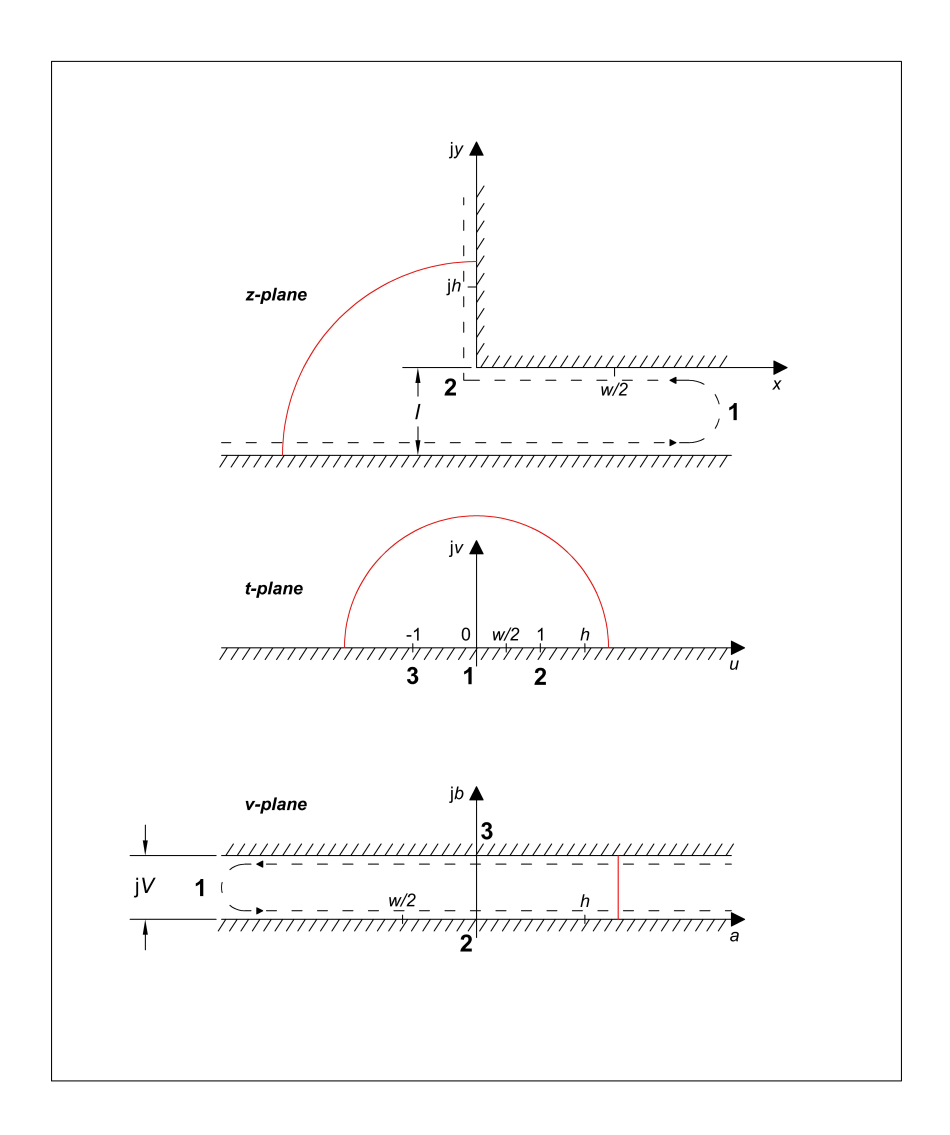


Figure 2.6: Schwarz-Christoffel mapping on the tooth geometry, in red a fringing flux line

The condition z(1)=0 leads to C=0. The second condition assumed is $z(t\to 0)=\infty$. To evaluate this limit, Eq. (2.35) must be integrated by using a change of variables. Specifically, the substitution $t=\epsilon e^{j\theta}$ is applied, where ϵ is an arbitrarily small positive number, and θ represents

the angle of the flux lines near the origin, with $\theta \in [0, \pi]$. Under this substitution, the differential becomes $dt = j\epsilon e^{j\pi} d\theta$.

Thus, for $t \rightarrow 0$, Eq.(2.35) becomes:

$$dz = K \frac{j}{t} dt = j K_1 \frac{j \epsilon e^{j\theta} d\theta}{\epsilon e^{j\theta}} = -K_1 d\theta$$
 (2.37)

Near t = 0, z varies from x - jl to x, while θ varies from π to 0. The integral of the previous Eq. (2.37) yields:

$$\int_{x-i}^{x} dz = \int_{\pi}^{0} -K_1 d\theta \tag{2.38}$$

Therefore,

$$jl = K_1 \pi \tag{2.39}$$

And

$$K_1 = j\frac{l}{\pi} \tag{2.40}$$

Substituting the values of C_1 and K_1 in Eq.2.36 leads to the following transformation equation:

$$z(t) = \frac{l}{\pi} (2\ln(1+\sqrt{1-t}) - \ln(t) - 2\sqrt{1-t})$$
(2.41)

From the t-plane to the v-plane

To easily compute the 2D reluctance, a new mapping must be performed. The new mapping that transforms the t-plane into the v-plane must be implemented following Eq.(2.34) and the geometry depicted in Fig. 2.6, following the same analytical steps of the previous transformation.

The Schwarz-Christoffel differential equation applied in this case is the following:

$$\frac{dv}{dt} = \frac{K_2}{t} \tag{2.42}$$

Integrating both sides yields:

$$v(t) = K_2 \ln t + C_2 \tag{2.43}$$

The two constants K_2 and C_2 must be derived considering the boundary conditions v(1) = 0 and v(-1) = jV. The first condition gives $C_2 = 0$. The second, instead, leads to the following equality:

$$jV = K_2 \ln - 1 = K_2 j\pi \tag{2.44}$$

Therefore,

$$K_2 = \frac{V}{\pi} \tag{2.45}$$

The transformation equation yields to

$$v(t) = \frac{V}{\pi} \ln t \tag{2.46}$$

2.3.2 Reluctance calculation

Once the two transformation equations that map the geometry from the v-plane to the t-plane and from the t-plane to the z-plane are derived, it is possible to define the reluctance in the v-plane and then transform back its expression onto the z-plane.

From the geometry depicted in Fig. 2.6, the 2D reluctance can be easily computed as follows.

$$\mathcal{R} = \frac{V}{\mu_0(h_\nu - (\frac{w}{2})_\nu)} \tag{2.47}$$

Where h_v and $(\frac{w}{2})_v$ represent, respectively, the height of the slot and half of the tooth width expressed in the v-plane.

Their values must therefore be determined using the previously derived transformations, starting from the z-plane.

Expression of h_v

To compute h_{ν} , Eq. (2.41) must be considered. Under the assumption of $t \to \infty$, which physically corresponds to the air gap width being negligible compared to the height of the tooth, the equation simplifies as follows:

$$z(t) = 0 + jy = \frac{l}{\pi} (2\ln(1 + \sqrt{1 - t}) - \ln(t) - 2\sqrt{1 - t})$$
(2.48)

$$= \frac{l}{\pi} \left(\ln(-1) + 2j\sqrt{t} \right) \tag{2.49}$$

$$=j\frac{l}{\pi}\left(\pi+2\sqrt{t}\right)\tag{2.50}$$

For $t \to \infty$, the factor $(\pi + 2\sqrt{t}) \approx 2\sqrt{t}$ and the previous expression can be rewritten as

$$\sqrt{t} = \frac{\pi y}{2I} \tag{2.51}$$

Therefore,

$$t = \left(\frac{\pi y}{2l}\right)^2 \tag{2.52}$$

Considering now the second transformation, i.e., Eq. 2.46, and imposing y = h, the value of h_v can be derived.

$$h_{v} = \frac{V}{\pi} \ln t = \frac{2V}{\pi} \ln \frac{\pi h}{2l}$$
 (2.53)

Expression of $\left(\frac{w}{2}\right)_{\nu}$

The second variable to be determined is $\left(\frac{w}{2}\right)_v$. In this case, $t \approx 0$ and Eq. 2.36 becomes:

$$z(t) = x + j0 = \frac{l}{\pi} (2\ln(1 + \sqrt{1 - t}) - \ln(t) - 2\sqrt{1 - t})$$
(2.54)

$$= \frac{l}{\pi} (2 \ln 2 - \ln t - 2) \tag{2.55}$$

Therefore,

$$\ln t = -\frac{\pi x}{l} + 2(\ln 2 - 1) \tag{2.56}$$

Considering $x = \frac{w}{2}$ and substituting in Eq.2.46 leads to

$$\left(\frac{w}{2}\right)_{v} = \frac{V}{\pi} \ln t = \frac{V}{\pi} \left(-\frac{\pi w}{2l} + 2(\ln 2 - 1) \right)$$
 (2.57)

Expression of the reluctance

Finally, substituting the two values of h_v and $\left(\frac{w}{2}\right)_v$ in the 2D reluctance of Eq. 2.47 leads to the following expression:

$$\mathcal{R} = \frac{V}{\mu_0 \left[\frac{2V}{\pi} \ln \frac{\pi h}{2l} + \frac{V}{\pi} \left(\frac{\pi w}{2l} + 2(1 - \ln 2) \right) \right]}$$
(2.58)

$$= \frac{1}{\mu_0 \left[\frac{w}{2l} + \frac{2}{\pi} \left(1 + \ln \frac{\pi h}{4l} \right) \right]}$$
 (2.59)

2.3.3 Application of the Schwarz-Christoffel transformation to the electromagnet

To account for the decrease in reluctance due to fringing fluxes in a more complex geometry compared to that in Fig. 2.6, the new geometry must be decomposed so that the basic one can be used as a building block.

The 2D reluctance of the basic geometry is the one reported below:

$$\mathcal{R}'_{basic} = \frac{1}{\mu_0 \left[\frac{w}{2l} + \frac{2}{\pi} \left(1 + \ln \frac{\pi h}{4l} \right) \right]}$$
 (2.60)

Where w is the tooth width, l is the air gap length, and h is the slot height.

It has the dimensions of a per-unit-of-length permeance [m/H]. Taking into account the geometry of Fig.2.6 as a building block, the air gap geometry can be modeled as shown in Fig. 2.7.

In particular, for the air gap geometry of interest in this study, the real geometry can be modeled as a parallel of two of the basic geometry used in the Schwarz-Christoffel reluctance derivation.

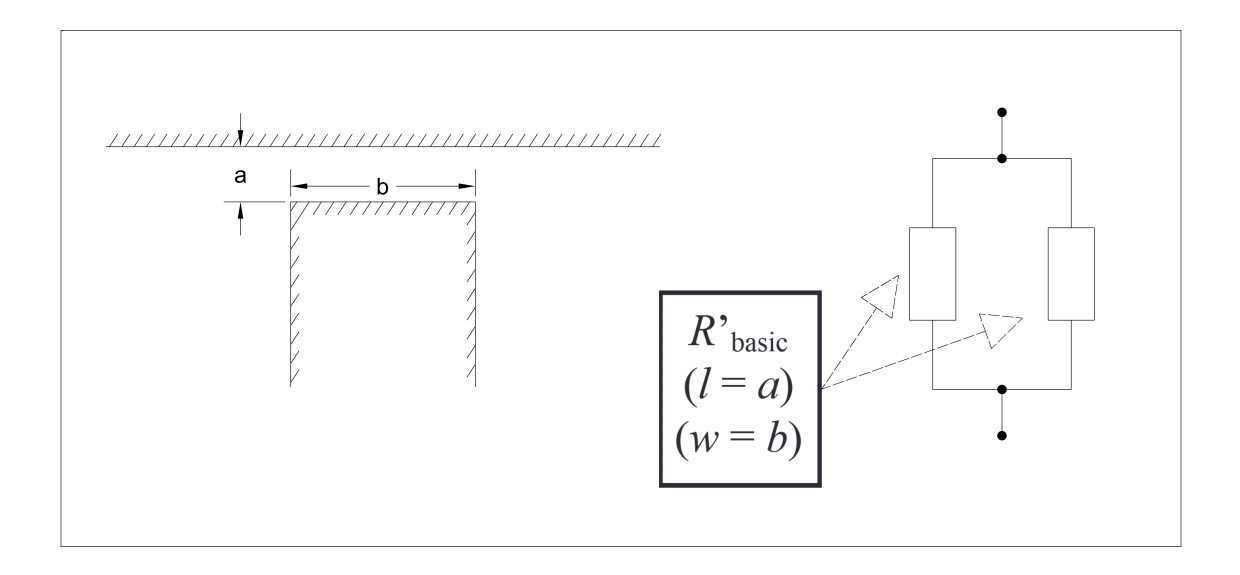


Figure 2.7: Construction of the total air gap reluctance

The final expression for the total 2D air gap reluctance is the following:

$$\mathcal{R}' = \frac{\mathcal{R}'_{basic}}{2} \tag{2.61}$$

The derivation of the correction factor for a 3D model is more challenging because it requires accounting for fringing fluxes in both the x and y directions.

For this reason, two fringing factors must be computed following the notation of Fig.2.8. Taking into consideration firstly the fringing fluxes in the y direction and normalizing the Schwarz-Christoffel reluctance with the 2D basic reluctance leads to the following fringing factor.

$$\sigma_z = \frac{\mathcal{R}'_{zy}}{\frac{\delta}{\mu_0 w}} \tag{2.62}$$

Similarly, the fringing factor in the x direction writes:

$$\sigma_x = \frac{\mathcal{R}'_{xy}}{\frac{\delta}{\mu_0 l}} \tag{2.63}$$

Finally, the total 3D reluctance that considers the presence of both fringing fluxes in the x and y directions is the following.

$$\mathcal{R}_{3D} = \sigma_x \sigma_z \frac{\delta}{\mu_0 \cdot w \cdot l} \tag{2.64}$$

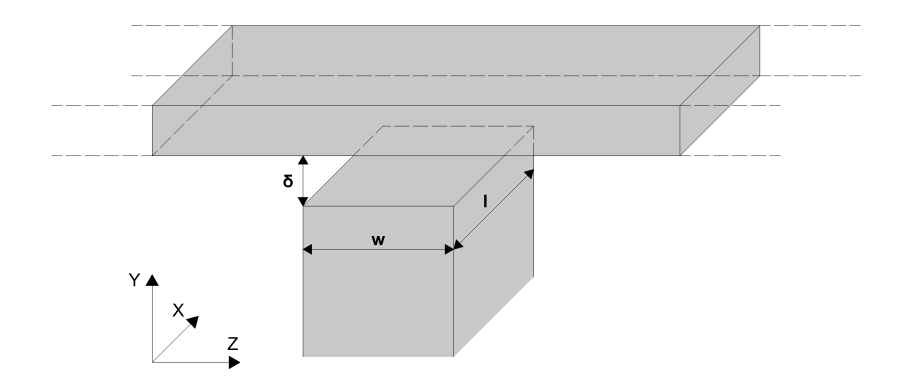


Figure 2.8: Geometry used to compute the fringing factors

The fringing factors in the *x* and *y* directions reduce the total reluctance of the air gap. Their inverses can also be interpreted as an effective increase in the cross-sectional area of the air gap, accounting for the presence of fringing fluxes.

The new air gap reluctance can be substituted in the expression of the inductance for the evaluation of the force, as explained in Section 2.1.4.

2.4 Infinite magnetic permeability hypothesis compensation

To correctly close the magnetic circuit, the reluctances of the ferromagnetic core must be added to those of the air gaps.

The reluctances related to the ferromagnetic core can be simply modeled using the definition provided in Eq. (2.14).

In formulas:

$$\mathscr{R} = \frac{l}{\mu_0 \mu_r S} \tag{2.65}$$

Where l is the length of the magnetic branch, S its cross-sectional area, and μ_r the relative magnetic permeability of the iron. Given that the relative permeability of iron is much higher than that of air, the magnetic flux can be assumed to remain entirely confined within the core material. Consequently, flux leakage can be neglected, and there is no need to refine the model, such as by introducing fringing corrections, as was done previously for the air gaps.

Moreover, due to the high magnetic permeability of the iron, the reluctances of the ferromagnetic core are considerably smaller than those of the air gaps. Therefore, any modeling inaccuracies in this part of the circuit have only a minor influence on the overall results.

2.5 Concluding remarks

In this chapter, a complete analytical model for the levitation electromagnet under stationary conditions has been derived.

The approach combines:

- The magnetic circuit method, relying on Hopkinson's laws, to capture the main flux paths and relate design parameters to the levitation force.
- The energy-based method for force computation, which links inductance variation to mechanical output.
- A Schwarz–Christoffel conformal mapping correction to accurately model fringing fluxes in the air gap, overcoming the limitations of empirical fringing factors.

The resulting model provides:

- Explicit expressions for the force and the specific force in terms of geometry and current density.
- An estimation of Joule losses and a loss-force ratio for early-stage optimization.
- A 3D reluctance formulation accounting for fringing in both transverse directions.

In the next chapter, this analytical formulation will be benchmarked against finite-element simulations to assess its predictive accuracy and to determine its applicability for design optimization.

Chapter 3

2D and 3D simulations in static conditions

In this chapter, the analytical models developed in the previous sections are validated through both 2D and 3D finite element simulations performed in COMSOL. The aim is to assess their predictive accuracy and determine which model, either the basic reluctance model or the one enhanced with the Schwarz–Christoffel correction for fringing fluxes, provides the closest match to numerical results.

The FEM simulations are based on the electromagnet geometry shown in Fig. 2.3, with the slot assumed to be completely filled with windings. This design choice maximizes the use of available space and increases the achievable energy density.

For comparison, a parametric approach was adopted in which one parameter was varied at a time while all others were kept fixed to the nominal values listed in Table 3.1. This method isolates the effect of each parameter and facilitates a direct evaluation of how analytical models respond to changes in geometry or operating conditions.

Parameters	Values
1	0.1 [<i>m</i>]
δ	1 [<i>mm</i>]
W	12 [<i>mm</i>]
b	50 [<i>mm</i>]
h	30 [<i>mm</i>]
a	10 [<i>mm</i>]
J	$2 [A/mm^2]$
N	20

Table 3.1: Electromagnet parameters for model comparison

3.1 COMSOL models

3.1.1 Definition of the problem

The COMSOL models were developed using the parameters listed in Table 3.1 from the previous section

For both the 2D and 3D stationary models, the *Magnetic Fields* physics interface was employed. In each domain, the *Ampère's Law in Solid* condition was applied, ensuring that the following set of equations is satisfied:

$$\begin{cases} \vec{\nabla} \times \vec{H} = \vec{J} & \text{(Ampère's law)} \\ \vec{\nabla} \times \vec{A} = \vec{B} & \text{(Definition of magnetic vector potential)} \\ \vec{J} = \sigma \vec{E} & \text{(Ohm's law for conductors)} \end{cases}$$
(3.1)

These equations form the basis of magnetostatic modeling in COMSOL. The *Ampère's Law in Solid* domain also permits modification of the **constitutive relations** for magnetic and electric fields. Since the aim here is to validate the analytical models under their original assumptions, **linear constitutive laws** were adopted, matching the analytical framework:

$$\begin{cases} \vec{B} = \mu_0 \mu_r \vec{H} & \text{(Magnetic constitutive relation)} \\ \vec{D} = \epsilon_0 \epsilon_r \vec{E} & \text{(Electric constitutive relation)} \end{cases}$$
(3.2)

The coil was modeled using the *Coil* domain feature, where the current and number of turns were explicitly defined. This yields a uniform current density distribution in the winding region, consistent with the analytical model.

The *Force calculation* feature was applied either to the yoke or to the rail. According to Newton's third law, the magnitudes of these forces must be equal, with opposite directions.

For both the 2D and 3D cases, a **direct solver** was used by default, which inverts the system matrix through LU decomposition, an efficient and robust choice for well-conditioned problems. Alternatively, COMSOL offers an **iterative solver** (conjugate gradient method), which progressively refines the solution. This method is computationally cheaper for large systems and also provides useful feedback on convergence behavior:

- *Monotonic convergence* generally indicates a well-conditioned model.
- Oscillatory convergence may suggest poor model definition or insufficient constraints in the geometry or physics setup.

3.1.2 2D COMSOL model

The 2D COMSOL model serves as a valuable tool for preliminary analysis, providing a good approximation of the magnetic behavior while avoiding the computational complexity associated with a full 3D simulation. This efficiency is achieved by using elements with simpler shape functions and a reduced number of nodes, which significantly decreases simulation time.

However, the 2D approach has inherent limitations. In particular, it cannot capture:

- Edge effects occurring along the longitudinal (out-of-plane) direction.
- The presence and influence of the coil heads, which contribute to the total mass and can alter the magnetic field distribution near the coil ends.

The model geometry and the corresponding magnetic flux density distribution are shown in Fig. 3.1 and Fig. 3.2, respectively. In the flux density plot, blue regions correspond to lower $\|\vec{B}\|$ values, whereas red areas indicate higher flux density, especially concentrated near the coils.

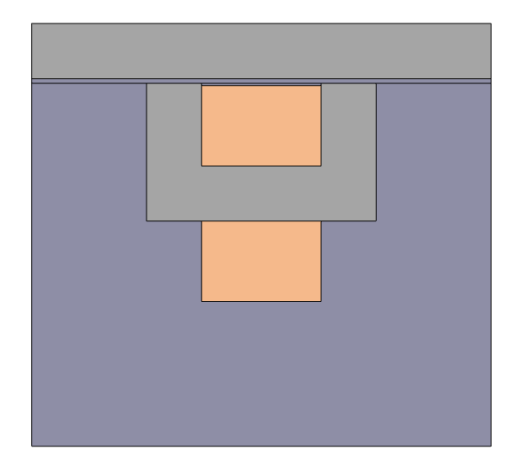


Figure 3.1: Geometry of the 2D COMSOL model

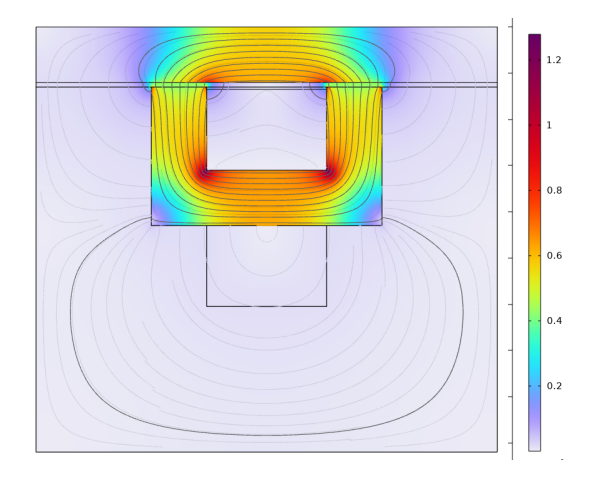


Figure 3.2: Magnetic flux density distribution $\|\vec{B}\|$ in the 2D COMSOL simulation

3.1.3 3D COMSOL model

The 3D COMSOL model was developed using the *3D Magnetic Fields* physics interface. Compared to the 2D approach, it provides a more accurate representation of the electromagnetic problem, as it naturally accounts for three-dimensional effects such as:

- Edge effects along all directions.
- The influence of coil heads on the overall magnetic circuit and total mass.
- Non-uniform field distributions along the longitudinal axis.

This improved accuracy comes at the expense of significantly higher computational demands, as shown in Table 3.2, which compares simulation times for the analytical model, the 2D FEM model, and the 3D FEM model.

Figures 3.3 and 3.4 show the 3D model geometry and the corresponding simulated magnetic flux density distribution $\|\vec{B}\|$, respectively.

	Analytical	2D FEM	3D FEM
Simulation time	~ 1 s	~ 20 s	~ 10 min

Table 3.2: Comparison of simulation times for the analytical model, 2D FEM, and 3D FEM simulations

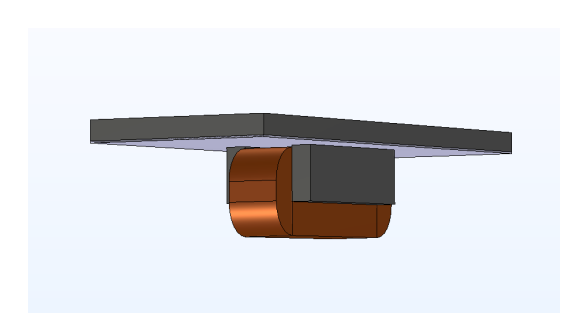


Figure 3.3: Geometry of the 3D COMSOL model

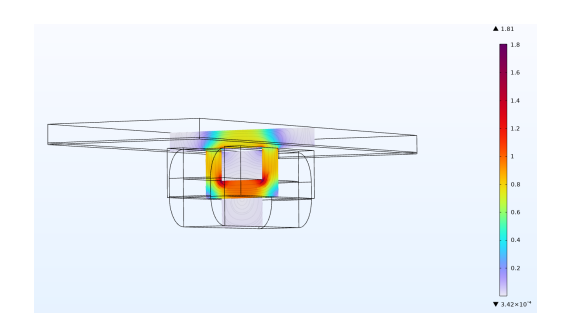


Figure 3.4: Magnetic flux density distribution $\|\vec{B}\|$ in the 3D COMSOL simulation

3.1.4 Materials

In COMSOL simulations, the choice of materials directly affects the computed electromagnetic behaviour, since their physical properties determine both magnetic performance and electrical losses. For instance, modifying the coil material changes its electrical resistivity, directly influencing Joule losses P_J . Or instead, changing the yoke or rail material alters the magnetic circuit's reluctance and its saturation characteristics.

For the present study, the following materials from the COMSOL library were assigned:

- *Soft Iron* (linear), with relative magnetic permeability $\mu_r = 4000$, for both the rail and the yoke. This value ensures a high magnetic conductivity while avoiding saturation in the considered operating range.
- *Copper* for the coil windings, due to its low electrical resistivity, thus minimizing Joule losses for a given current density.
- *Air* for the remaining regions.

The assumption of linear μ_r was made deliberately, to ensure full consistency between the FEM simulations and the analytical models developed earlier, which also neglect nonlinear saturation effects. This allows a direct and fair comparison between the two approaches.

3.1.5 Mesh convergence study

To ensure the reliability of the FEM results, a mesh convergence study is essential. An overly coarse mesh may contain elements too large to accurately resolve spatial variations of the electromagnetic field, leading to significant numerical error. Conversely, an excessively fine mesh increases computational time without proportionate gains in accuracy.

The objective of this study is therefore to find an optimal trade-off between result accuracy and computational cost.

For the 2D model, the simulation time remains low even when using a fine mesh (see Table 3.2). Therefore, a mesh convergence analysis is not strictly necessary in this case, as the computational penalty of refining the mesh is negligible.

For the 3D simulations, the situation is different: computation times are already substantial, even with a relatively coarse mesh. A progressive mesh refinement was performed, from "Extremely coarse" to "Extremely fine", and the computed levitation force was monitored as the convergence metric.

The optimal mesh is identified at the so-called "knee" of the convergence curve in Fig.3.5, i.e., the point beyond which further refinement produces only marginal improvements in accuracy while significantly increasing computation time.

The mesh parameters for each refinement level are summarized in Table 3.3. Based on the results, the "Fine" mesh offers an excellent compromise between computational effort and accuracy: finer meshes produce negligible improvements in the force, while coarser meshes lead to measurable deviations from the converged value.

Both the 2D and 3D models employed the *Free Tetrahedra* mesh. For the purposes of this stationary validation study, this element type provided acceptable accuracy. However, in the dynamic analyses presented in Chapter 6, a more refined and targeted mesh is required to ensure solver convergence and numerical stability.

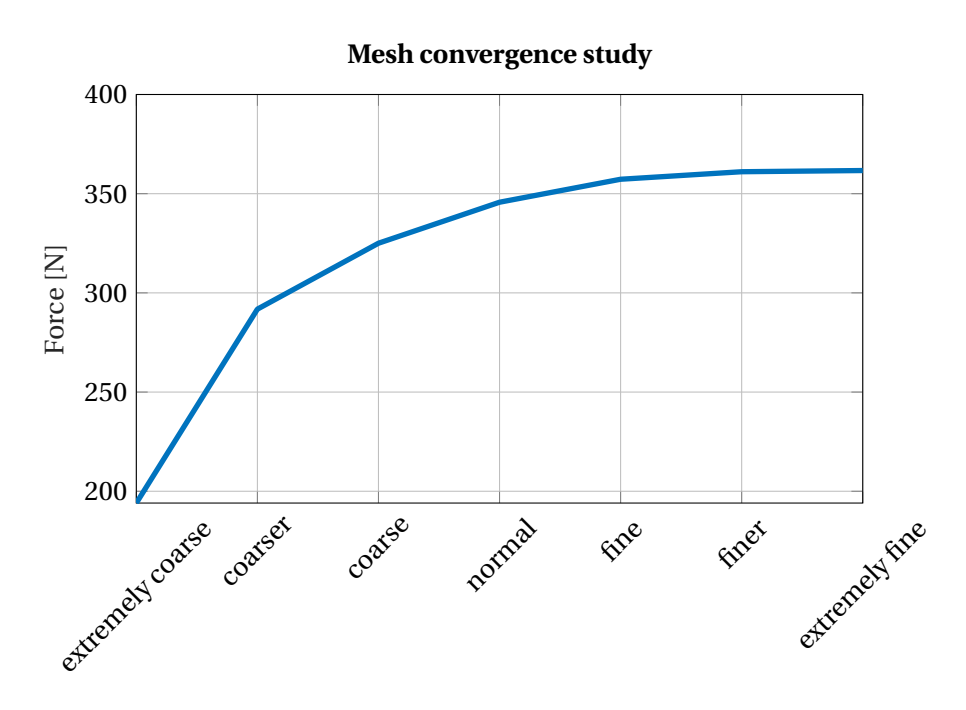


Figure 3.5: Mesh convergence study: levitation force F_{lev} as a function of element size

	Extremely coarse	Coarser	Coarse	Normal	Fine	Finer	Extremely fine
Max. element size [mm]	325	124	97.5	65	52	35.8	13
Min. element size [mm]	45.5	26	18.2	11.7	6.5	2.6	0.13
Max. element growth rate	2.0	1.7	1.6	1.5	1.45	1.4	1.3
Curvature factor	1.0	0.8	0.7	0.6	0.5	0.4	0.2
Resolution of narrow regions	0.1	0.3	0.4	0.5	0.6	0.7	1.0

Table 3.3: Mesh parameters for different refinement levels

3.2 Simulation results

Once the COMSOL geometries for both the 2D and 3D cases were defined, a series of simulations was carried out to compare the results with those obtained from the analytical models. The comparison was performed by varying one parameter at a time, while keeping all others fixed, using the *Sweep* functionality in COMSOL.

3.2.1 Error metric

To quantify the accuracy of the analytical predictions, the Relative Error (RE) over all sweep points was computed as:

$$e = \frac{|F_{\rm C} - \hat{F}|}{F_{\rm C}},\tag{3.3}$$

where F_C is the force computed from the COMSOL simulation and \hat{F} the force predicted by the analytical model.

A low value of *e* indicates a close agreement between analytical and FEM results.

3.2.2 Comparison between the 2D analytical and COMSOL models

The first set of tests involved varying the air gap width δ of the electromagnet.

Simple reluctance model

For the basic reluctance model (no fringing correction), the results are shown in Fig.3.6. As expected from Eq.(2.23), the force decreases approximately quadratically with increasing air gap width. However, the relative error grows with δ due to the conservative assumption that the magnetic flux remains strictly orthogonal to the yoke cross-section.

In this case, the error increases from $\approx 5\%$ at $\delta = 1$ mm to over 25% at $\delta = 5$ mm.

Schwarz-Christoffel correction

Applying the Schwarz-Christoffel conformal mapping correction significantly improves the match with FEM results (Fig. 3.7). Here, the error remains nearly constant for small air gaps and increases only moderately for larger ones, reaching values roughly half of those of the simple model. This improvement stems from the conformal mappings ability to account for fringing fluxes more accurately.

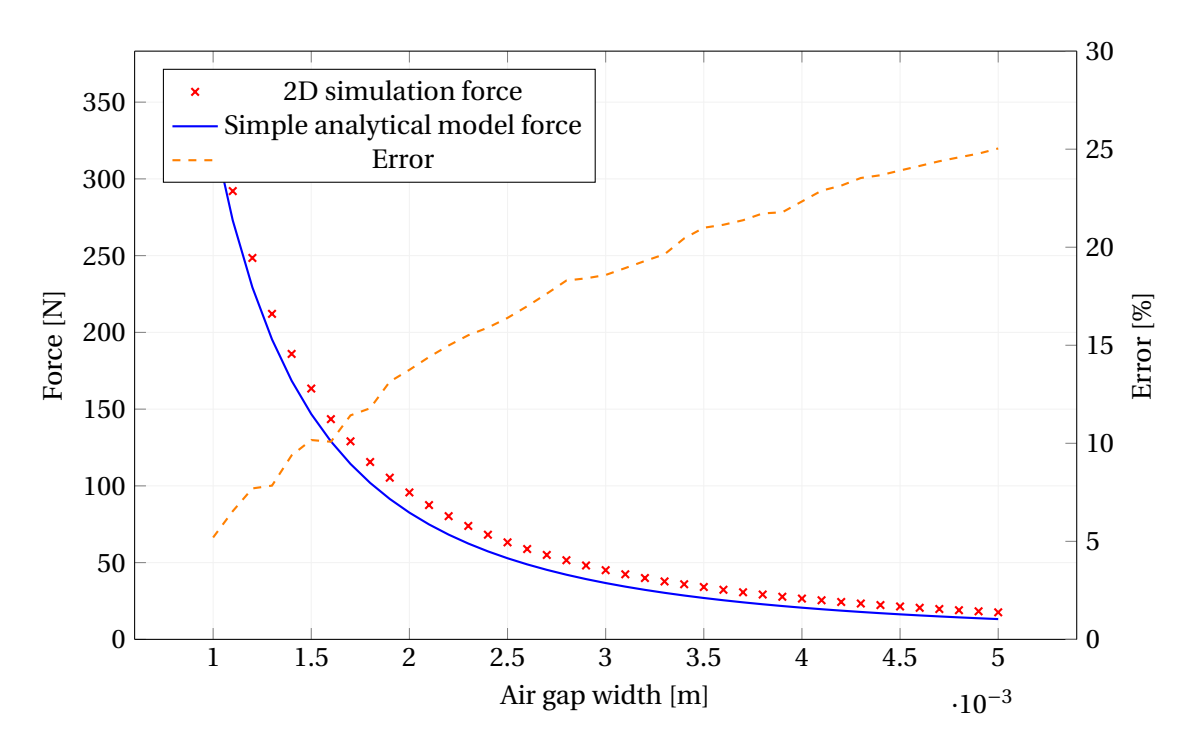


Figure 3.6: Force changing the air gap width: simple reluctance model vs. 2D FEM

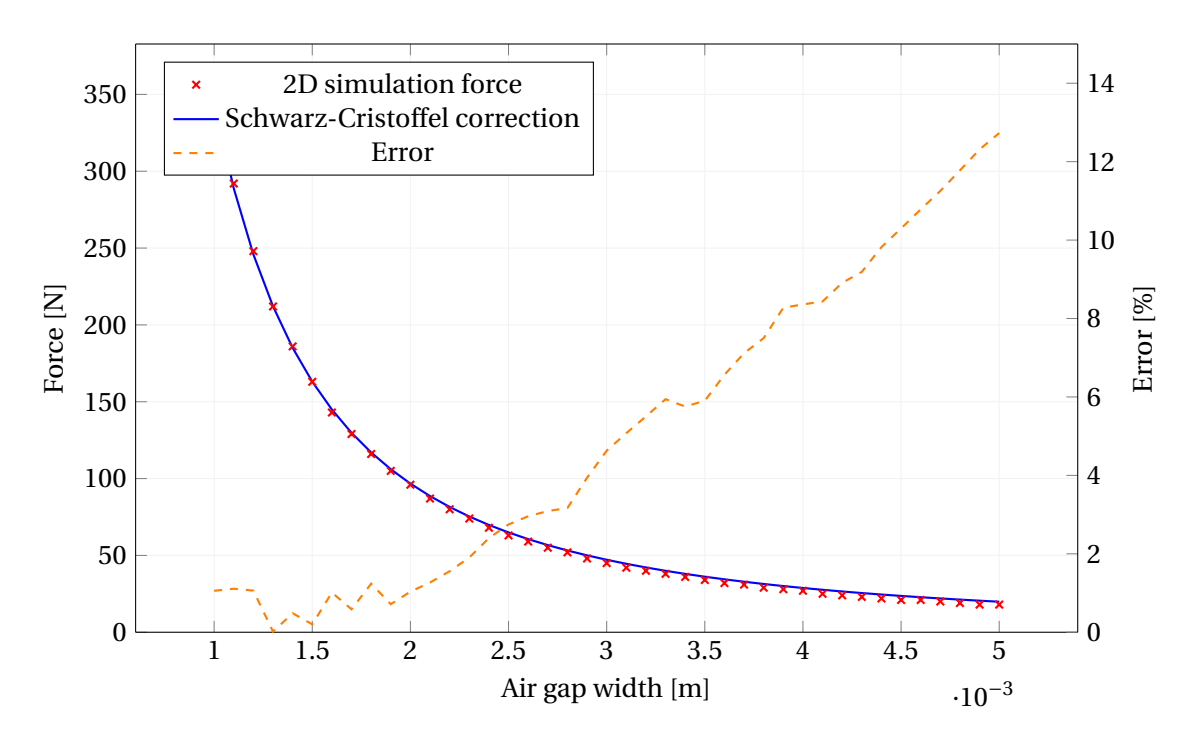


Figure 3.7: Force changing the air gap width: Schwarz-Christoffel correction vs. 2D FEM

3.2.3 Comparison between the 3D analytical and COMSOL models

The same analysis was repeated for the 3D case, with mesh parameters validated in the previous section. As in the 2D case, the Schwarz-Christoffel correction consistently outperformed the simple reluctance model, achieving a mean relative error of approximately 5% across the tested range of δ (Fig.3.8).

Small oscillations in the error curve can be attributed to meshing effects: slight changes in δ modify the number and distribution of elements in the *Free Tetrahedra* mesh, introducing small numerical variations in F_C .

Overall, including fringing fluxes in the analytical formulation significantly improves predictive accuracy, fully justifying the use of the Schwarz-Christoffel mapping.

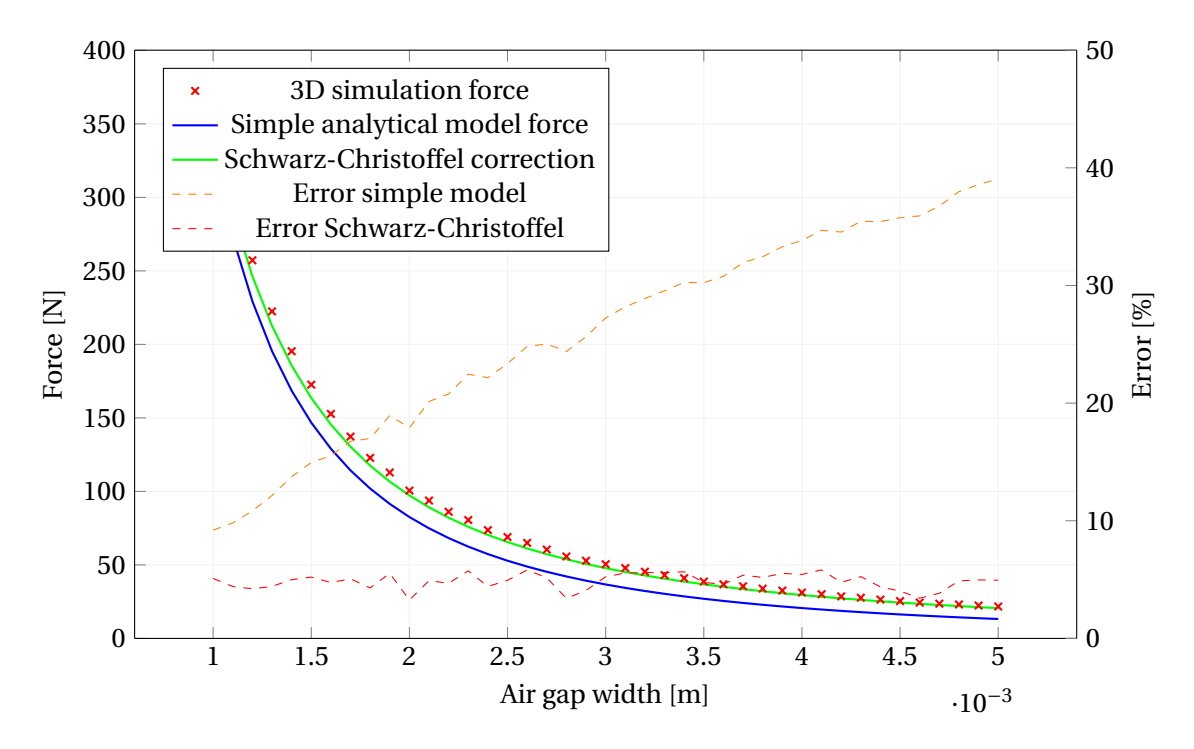


Figure 3.8: Comparison between the force generated by the analytical models and the 3D simulations

In Fig. 3.8, the error between the simple reluctance model and the simulations is double that of the 2D case. This is caused by the presence of the fringing fluxes in the longitudinal direction, which are instead considered in the Schwarz-Christoffel formulation.

The validated analytical model can therefore be confidently applied in optimization studies, ensuring that, even for varying δ , the error relative to FEM results remains below $\approx 5\%$.

3.3 Comparison varying other dimensions

To further validate the analytical model, additional comparisons were carried out by varying each geometrical or physical parameter of the electromagnet individually. The following performance metrics were used:

- The *specific force*, defined in Eq. (2.22), which measures the generated force per unit weight.
- The *losses-to-force ratio*, defined in Eq.(2.28), which quantifies Joule losses per unit of generated force.

This dual metric approach reflects the main design objective: maximizing the specific force while minimizing the energy cost per unit of force. Unless otherwise stated, the analytical predictions are obtained using the 3D model corrected with the Schwarz–Christoffel mapping. Error values are not explicitly tabulated here, as they remain within the $\approx 5\%$ range established in the air gap comparison.

3.3.1 Variation in length l

In the first study, the length l of the electromagnet was varied while keeping all other parameters fixed.

In the 2D simulations, both the total force and the total weight scale linearly with l, making the specific force independent of length, as expected from Eq.(2.22).

The 3D simulations display an increasing specific force with l, approaching the 2D value asymptotically. This difference arises from the coil heads: their weight contribution becomes relatively smaller as l increases, improving the force-to-weight ratio.

For both 2D and 3D cases, the loss-to-force ratio remains essentially constant, as increasing l proportionally increases both winding resistance and generated force (Eq.(2.28)).

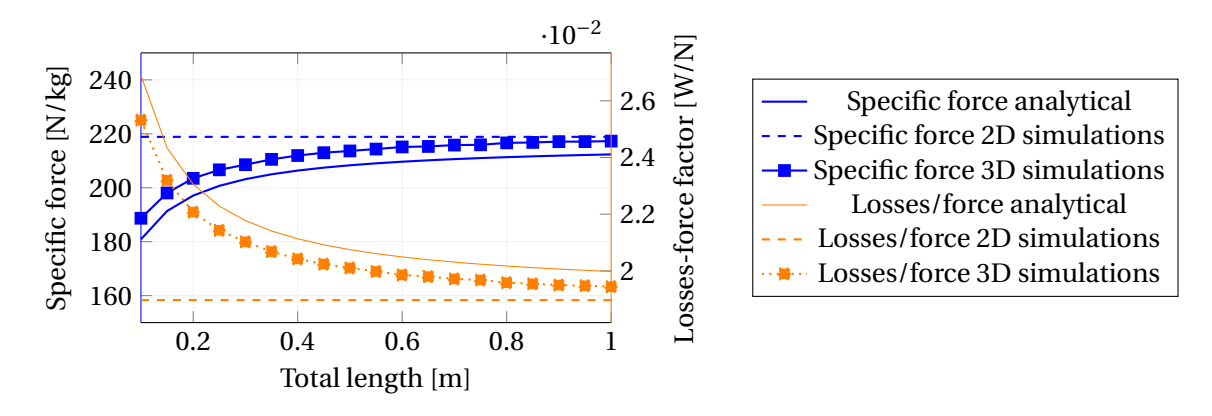


Figure 3.9: Effect of length *l* on specific force and losses-to-force ratio

3.3.2 Variation in tooth width w

In this case, the tooth width w was varied while keeping the total width b constant.

An optimal ratio $\epsilon = w/b$ exists that maximizes the specific force. From Eq.(2.22), setting $\frac{\partial f_{\text{spec}}}{\partial w} = 0$ yields this optimum analytically. For the parameters in Table 3.1, $\epsilon_{\text{opt}} \approx 0.13$.

The 2D model consistently predicts higher specific forces than the 3D model and analytical prediction, due to the absence of coil heads in 2D (lower total mass for the same active length). The optimum ϵ may shift if nonlinear magnetic effects (e.g., saturation) are included.

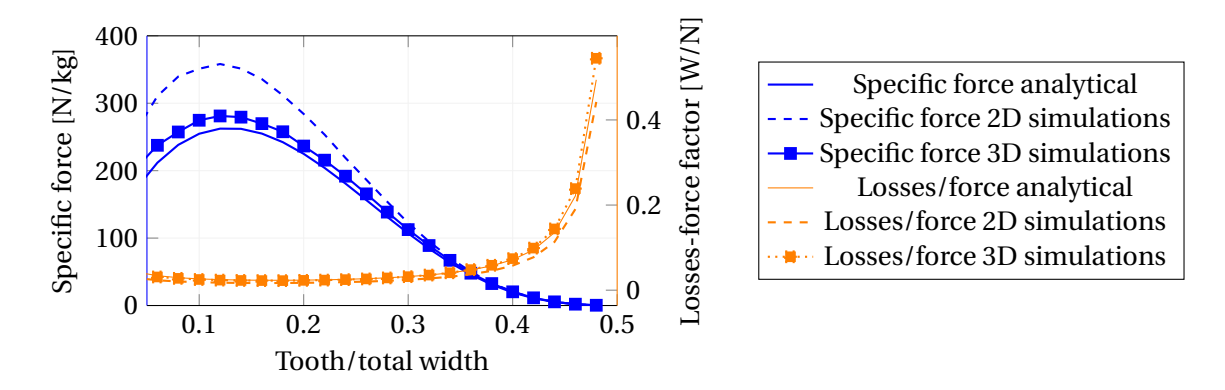


Figure 3.10: Effect of tooth width w on specific force and losses-to-force ratio

3.3.3 Variation in current density *J*

Finally, the effect of varying the current density J in the windings was analyzed. Both quantities scale approximately as J^2 , consistent with the Lorentz force dependence on current. The losses-to-force ratio remains constant with J, since both Joule losses P_J and generated force scale quadratically with current density.

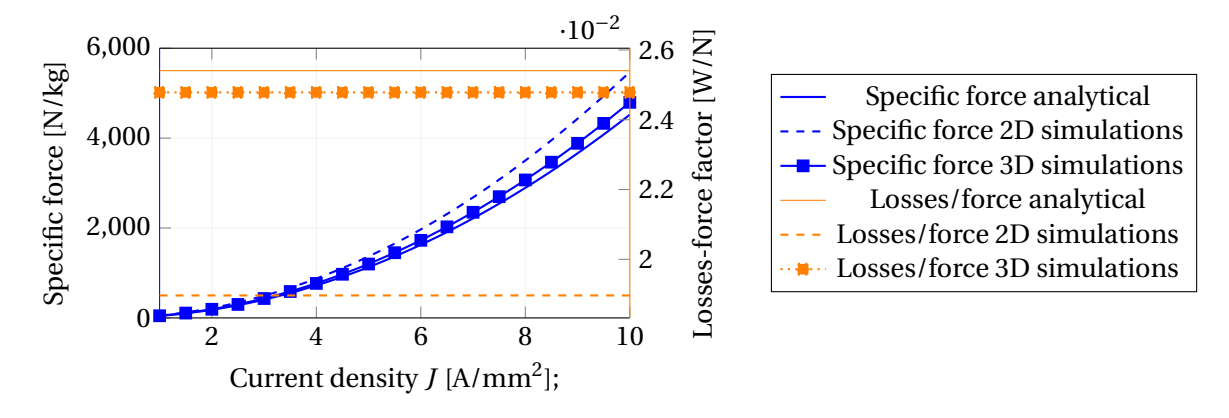


Figure 3.11: Effect of current density *J* on specific force and losses-to-force ratio

3.4 Conclusion remarks and practical implications

The validation study confirms that the analytical model, when corrected using the Schwarz-Christoffel conformal mapping, provides highly accurate predictions of the levitation force for the electromagnet in stationary conditions. Across all tested geometries and operating points, the mean relative error remained below approximately 5%, which is well within the acceptable range for preliminary design and optimization work.

3.4.1 Key observations

- The largest deviations between the basic reluctance model and the FEM results occur when varying the air gap, due to the increase of fringing fluxes.
- The Schwarz–Christoffel correction substantially reduces these deviations by correctly modeling the field distribution in the gap region.
- Table 3.4 highlights the improvement in prediction accuracy achieved by including the correction term.

Parameter varied	Range tested	Mean error – simple model	Mean error – S.C. corrected	
Air gap	1-5 [mm]	10–39 %	≈ 5 %	

Table 3.4: Summary of validation results for air gap variation

3.4.2 Computational efficiency

A key advantage of the analytical approach is its extremely low computational cost compared to FEM simulations. Table 3.5 reports typical simulation times for the analytical model, the 2D FEM model, and the 3D FEM model.

Model	Simulation time	Speed-up vs. 3D FEM
Analytical	~ 1 s	~ 600×
2D FEM	~ 20 s	~ 30×
3D FEM	~ 10 min	Reference

Table 3.5: Comparison of computational costs

This efficiency enables rapid parameter sweeps and geometry optimization without the need for high-performance computing resources, while still maintaining an accuracy of around 5% relative to 3D FEM results.

3.4.3 Recommended modeling workflow

Based on the results of this chapter, the following tiered approach is recommended for future design studies:

- 1. **Preliminary optimization:** Use the analytical model with the Schwarz-Christoffel correction for rapid evaluation of multiple design candidates.
- 2. **Intermediate verification:** Validate promising configurations using 2D FEM simulations, which balance computational time and accuracy.
- 3. **Final validation:** Perform full 3D FEM simulations to capture edge effects, coil head contributions, and any three-dimensional field non-uniformities.

This workflow ensures a good compromise between design speed and result reliability, while limiting reliance on computationally expensive simulations.

Chapter 4

Geometry optimization

4.1 Generalities

In this chapter, an alternative approach to that presented in [17] is introduced, aimed at identifying the optimal parameters for the design of the electromagnet. The analytical model has been validated through comparison with COMSOL simulations and can therefore be employed to investigate the optimal geometry for the electromagnet, i.e., the configuration that yields the highest levitation force under a given constraint on power losses. This investigation can be carried out either through analytical reasoning based on the force equation or by formulating a design optimization problem, in which an objective function is minimized subject to both geometric and physical constraints. The latter approach is more formal and flexible, as the optimization formulation can be easily modified to accommodate new requirements or constraints.

A general optimization problem can be defined as follows:

$$\min_{\bar{x}} \quad f(\bar{x})$$
s.t.
$$G(\bar{x}) \le 0,$$

$$H(\bar{x}) = 0$$

Here, \bar{x} denotes the vector of decision variables, $f(\bar{x})$ is the objective function to be minimized, subject to inequality constraints $G(\bar{x}) \leq 0$ and equality constraints $H(\bar{x}) = 0$. In the case of the electromagnet, the optimization problem includes non-convex and non-linear objective functions and constraints. As a result, the global optimum cannot be guaranteed from any arbitrary starting point due to the non-convex nature of the problem. A practical approach is to explore the solution space by initializing the gradient descent method from multiple starting points and selecting the best local minimum, i.e., the one yielding the lowest value of the objective function.

Furthermore, since the design requires maximizing the electromagnetic force while minimizing

Joule losses, the problem must be formulated as a multi-objective optimization. A common strategy is to use the weighted sum method, in which a Pareto-optimal solution can be obtained for each value of the weight parameter α in the objective function $Obj = -(F - \alpha \cdot P_J)$. An alternative approach is the ε -constraint method, where the force is maximized while treating Joule losses as a constraint. For each value of ε , the optimization problem is solved to find the maximum achievable force. Each solution then corresponds to a point on the Pareto front, representing a specific trade-off between force and losses. Although the two formulations are theoretically equivalent and lead in theory to the same set of Pareto-optimal solutions, the ε -constraint method often proves to be computationally more efficient and numerically more stable. The Pareto optimality is not straightforward and deserves a clearer explanation. In general, in multi-objective optimization, the Pareto optimal solution is the one that outperforms all the other options, i.e., it is impossible to improve one variable without harming other variables.

The conceptual algorithm used to initialize the random search in the solution space and to extract the Pareto front is outlined below.

Algorithm 1

Conceptual Algorithm to Solve the Optimization Problem

```
1: input: f(\bar{x}), G(\bar{x}), H(\bar{x})
 2: output: \min_{\bar{x}} f(\bar{x})
 3: for \varepsilon_i \in [\varepsilon_{min}, \varepsilon_{max}] do
           for i=1:200 do
 4:
                 initialize \bar{x}_0 = \bar{x}_{lb} + rand(0,1) \cdot (\bar{x}_{ub} - \bar{x}_{lb})
 5:
                 add constraint G(\bar{x}) + P_I \le \varepsilon_i
 6:
                 solve \Omega = fmincon(f(\bar{x}), \bar{x}_0, [], [], [], \bar{x}_{lb}, \bar{x}_{ub}, [G(\bar{x}) H(\bar{x})])
 7:
                 if \Omega_{i+1} \leq \Omega_i then
 8:
 9:
                       f_{opt} = \Omega_{i+1}
                 end if
10:
           end for
11:
           return F_{opt}(\varepsilon_i) = f_{opt}
12:
13: end for
```

Where $G(\bar{x})$ and $H(\bar{x})$ are respectively the inequality and equality constraints of the optimization problem, as shown before. The two vectors \bar{x}_{ub} and \bar{x}_{lb} represent, respectively, the upper and lower bounds for the decision variables. Therefore, the initial guesses for the gradient descent method are selected randomly from the feasible space. This approach is required due to the non-convexity and non-linearity of the problem. Initializing the gradient descent from only one feasible point can lead to a local minimum, and therefore, to a local optimal solution. Performing a random search in the entire solution space can better approximate the global optimum. The best objective value is selected iteratively by comparing the solution for every initialization step with the previous best

solution. Then the inner loop is repeated for every value of ε to find the Pareto optimal solutions.

4.2 Design optimization

The optimization problem for the design of the electromagnet is shown below, where the objective of the problem is the maximization of the levitation force (or the minimization of the force changed of sign). The constraints represent both the geometrical and physical limitations that the optimization problem must respect. In this sense, a good analytical model is fundamental to have the right approximation of the real levitation force generated. If the mathematical model gives results that aren't comparable with the real (or simulated) ones, the solution of the optimization will be inherently wrong. The optimization problem has been formulated as follows:

$$\min_{l,h,b,J,w,h_{coil},\varepsilon} -F$$
s.t. $0 \le l \le l_{max}$, $0 \le b \le b_{max}$, $0 \le h_{coil}$, $0 \le w$, $0 \le h$, $h + h_{coil} \le h_{max}$, $w + h_{coil} \le h$, $0 \le J \le 7 \frac{A}{mm^2}$, $0 \le B \le B_{max}$, $I = \frac{J \cdot h_{coil}(b-2w) \cdot F_f}{N}$, $I = \frac{\mu_0 NI}{2\delta}$, $I = \frac{\mu_0 NI}{2\delta}$, $I = \frac{\mu_0 NI}{2\delta}$, $I = \frac{\rho N^2 \cdot 2(I + w + \pi h_{coil}/2)}{h_{coil}(b-2w)F_f}$, $I = RI^2$, $I = RI$

Where F_f is the filling factor, δ is the air gap width, and N is the number of turns. The inductance L(x) is computed as explained in Section 2.1.4.

The constraints can be divided into different categories based on their utility:

- 1. The first seven inequalities represent the geometrical constraints and must be respected to make sure that the electromagnet can fit in the given chassis.
- 2. The constraint on the current density is used to ensure that the coils do not overheat; the maximum value for the current density is chosen to be $J = 7 \frac{A}{mm^2}$, which is high for an aircooled machine. However, it will be shown that the maximum value of current density is limited by the value of the losses constraint.
- 3. The constraint on the magnetic field is useful to ensure that the iron does not reach the saturation point. If that is the case, the constraint must be changed to consider also the non-linearities generated by the saturation.
- 4. All the equality constraints represent the physical equations that the problem must respect
- 5. Finally, the last inequality constraint is the implementation of the ε -constrained method. Varying ε and solving each time the optimization problem leads to the Pareto curve shown in the next section

The decision variables of the problem include both the geometry and the excitation parameters of the electromagnet. The final variable, denoted by ε , is specifically associated with the multi-objective optimization. Table 4.1 lists all the decision variables along with their corresponding physical meanings.

\	Length	Height	Width	Current density	Tooth width	Coil height	Epsilon constraint
Variable	l[m]	h [m]	b [m]	$J[A/mm^2]$	w [m]	$h_{coil}[m]$	$\varepsilon\left[W ight]$

Table 4.1: Decision variables

4.3 Optimal design

For the MATLAB implementation of the optimization problem, the Schwarz–Christoffel conformal mapping was used to define the mathematical model. As previously discussed, achieving an accurate approximation of the levitation force is essential to ensure the reliability of the optimization results. Among all the analytical approaches presented, the Schwarz–Christoffel method demonstrated the highest accuracy when compared to the COMSOL simulation results. Therefore, it was selected as the most suitable model to be used in the optimization process.

The explicit expression for the force computed with the correction is not reported here, but it can be derived from the magnetic coenergy (or energy, in the case of linear materials) by taking the derivative with respect to the air gap. This leads to an expression where the simple reluctance is replaced by the one obtained through the conformal mapping defined in Eq.2.64.

The following values were computed for the physical constraints related to the real-world application and listed in the introduction. In particular, $l_{max} = 0.35 \ m$, $b_{max} = 0.05 \ m$ and $h_{max} = 0.05 \ m$. By varying the constraint on the allowable power losses, ϵ , from 100J to 600J and solving the optimization problem for each value, the Pareto front shown in Fig.4.1 is obtained.

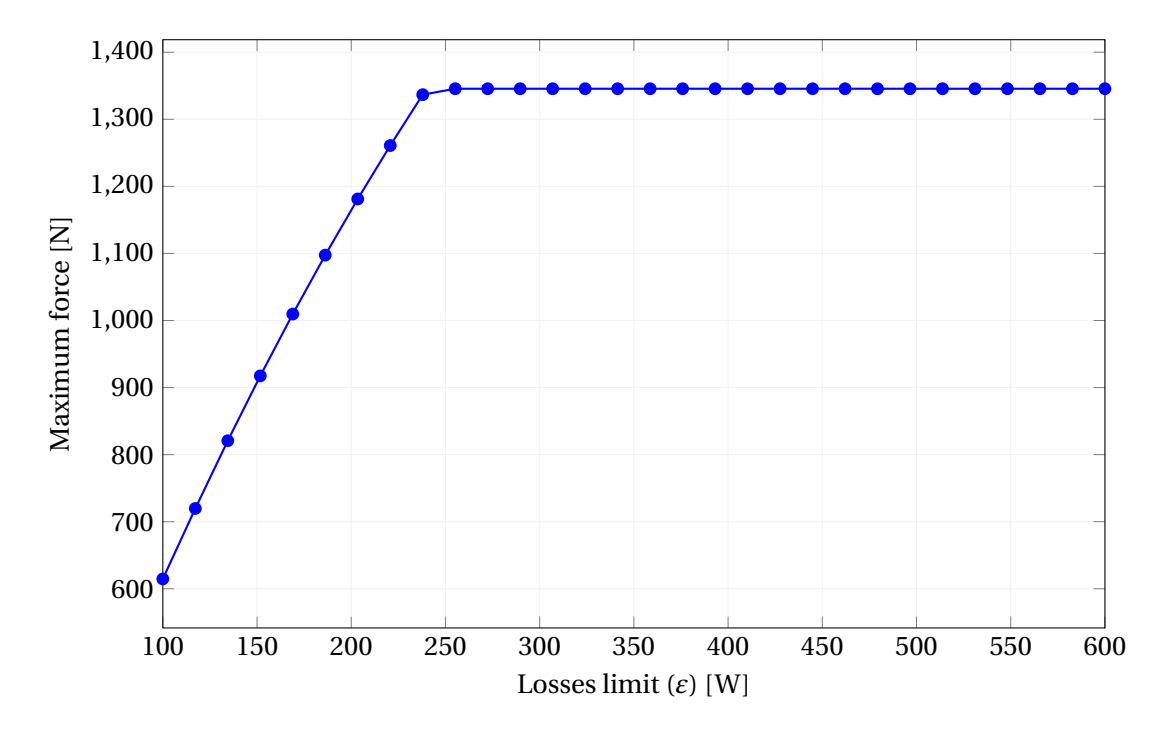


Figure 4.1: Pareto front

The optimal decision variables associated with the Pareto front are illustrated in Fig.4.2. As shown in the figure, increasing the current density leads to a wider tooth and consequently reduces the space available for the coils. This behavior is dictated by the constraint on the maximum magnetic flux density: as the current increases, so does the magnetic flux density in the yoke, which may approach the saturation limit of the ferromagnetic material. To prevent this, the optimization process prefers an increase in tooth width, which helps to reduce the local flux density. However, this design adaptation comes at the cost of reducing the available volume for the coils, thereby decreasing the achievable magnetomotive force. This trade-off reflects the balance enforced by the optimization between maximizing performance and respecting physical constraints.

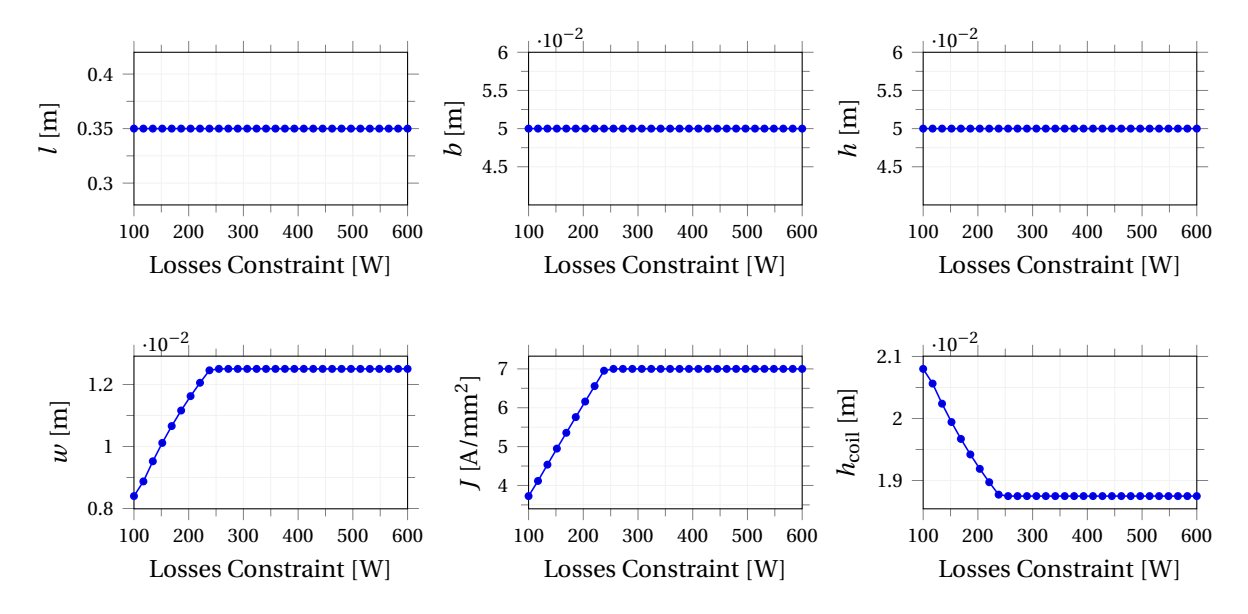


Figure 4.2: Optimal decision variables

4.3.1 Real-world application

To select the design to be tested using COMSOL simulations, it is necessary to account for the limitations in losses. As outlined in the introduction, one of the key design criteria for the electromagnet is that, at the nominal speed of 16m/s, the total losses must not exceed those associated with mechanical wheels. Under this constraint, the total power losses, defined as the sum of Joule losses and electromagnetic drag losses, must remain below a threshold of 250W per electromagnet.

Given this constraint, and considering that the required levitation force per electromagnet is approximately 500N, the selected design is the one reported in Table 4.2. This configuration satisfies both criteria based on analytical predictions, while taking a safety margin on the total levitation force.

In fact, the final validation must be performed through dynamic simulations, which will determine the levitation force and drag force at the nominal operating speed. If the results deviate from the requirements, the design can be iteratively refined to better satisfy them.

The COMSOL simulation confirms the analytical predictions: the total losses match exactly the ones computed analytically, while the FEM simulated levitation force F = 680N is slightly lower than the value computed using the Schwarz–Christoffel correction. However, the deviation remains within 5%, as expected from the comparisons performed in the previous chapter.

Parameters	Values		
δ	3 [<i>mm</i>]		
Length	0.35 [<i>m</i>]		
Tooth width	9 [<i>mm</i>]		
Total width	50 [<i>mm</i>]		
Yoke height	30 [mm]		
Coil height	20 [mm]		
J	$4.1 [A/mm^2]$		
Force	720 [<i>N</i>]		
Losses	117 [W]		

Table 4.2: Optimal electromagnet's parameters

4.4 Flexibility of the Optimization Problem

The optimization framework described in this chapter is inherently flexible and can be readily adapted to address alternative design objectives. For instance, if the goal shifts toward maximizing the specific force, this can be achieved by introducing an equality constraint on the total mass of the electromagnet and redefining the objective function to minimize the ratio between the generated force and the system's mass.

More generally, the problem formulation can be extended by incorporating additional constraints or by refining the analytical model used for force evaluation. One example would be to account for the effects of dynamic displacement of the electromagnet, as will be addressed in the subsequent chapters through the development of an enhanced dynamic model.

The core algorithm itself remains unchanged, as it is general enough to handle non-linear and non-convex problems. However, this generality comes at the cost of higher computational effort, particularly for problems with many local minima, since the solver must be initialized from multiple starting points. In simpler cases, such as convex and linear problems, this multi-start approach is unnecessary because every initial point converges to the same (and global) optimum. Nevertheless, the method outlined here ensures robustness across a broad spectrum of optimization problems, provided that the solver is initialized an appropriate number of times to adequately explore the solution space.

4.4.1 Concluding remarks

The optimization study presented in this chapter demonstrates the value of using a validated analytical model to rapidly explore the electromagnet design space. By adopting the ε -constraint multi-objective formulation, a Pareto front mapping the trade-off between levitation force and Joule losses is obtained.

From this analysis:

- The optimization revealed key design trade-offs, such as the balance between tooth width, coil space, and saturation limits.
- The selected real-world design satisfied both force and loss constraints, providing F = 680N with $P_J = 117W$ in COMSOL simulations.

This optimized configuration will serve as the baseline for the dynamic analysis in the following chapter, where the impact of speed-dependent effects on levitation and drag forces will be investigated.

Chapter 5

Analytical model in dynamic conditions

5.1 Introduction

In this chapter, an analytical model is developed to account for the displacement of the electromagnet. The objective is to support design optimizations that also consider the reduction in levitation force and the generation of drag force under dynamic operating conditions.

When the electromagnet moves and the rail is not laminated, high eddy currents are induced in the rail even at lower speeds. These currents produce their own magnetic field in the air gap, which interacts with the field generated by the excitation coil. The resulting superposition distorts the overall magnetic field distribution, leading to a reduction in levitation force and the appearance of a drag force opposing the motion.

The eddy currents restrict the penetration of the magnetic flux in the rail to a depth approximately equal to three times the skin depth, which depends on the electromagnet's displacement speed. Laminating the rail reduces this phenomenon but increases infrastructure costs.

The analytical model presented here builds on the early work of Yamamura (1970s) [18], but it is reinterpreted and updated. An improved drag-force formulation is also proposed, validated by comparison with FEM simulations.

This model is intended primarily as a preliminary design tool, to be subsequently verified and refined through numerical simulations.

5.2 Analytical model's derivation

5.2.1 Model' hypotheses and starting equations

To begin the derivation of the analytical model for the levitation loss and the drag force generation, several simplifying assumptions are introduced to reduce the complexity of the governing physics and equations:

• Uniform flux density across the air-gap width

$$\frac{\partial B(x, y, z)}{\partial y} = \frac{\partial^2 B(x, y, z)}{\partial y^2} = 0$$
 (5.1)

- · Constant electromagnet speed
- Constant DC excitation
- Linear and isotropic ferromagnetic properties

The first assumption enables a dimensional reduction of the problem, allowing the geometry to be simplified as illustrated in Fig. 5.1, where the field varies only in the x and z directions and is constant along y in the air gap.

The second and third assumptions allow transient effects to be neglected, focusing solely on steady-state conditions.

Finally, the assumption of linear ferromagnetic behaviour greatly simplifies the mathematical treatment, enabling the use of analytical tools that would be otherwise inapplicable under nonlinear conditions.

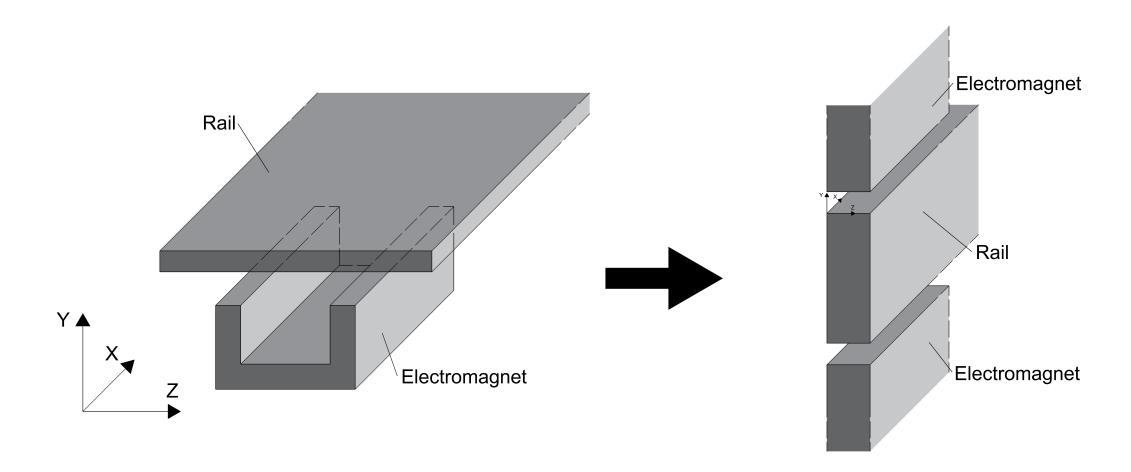


Figure 5.1: Geometry transformation to simplify the analytical derivation

Once the model assumptions have been established, the governing equations can be selected accordingly. The development of the analytical formulation begins with three fundamental relations: the generalized Ohm's law including the additional term accounting for currents induced by motion (Eq. 5.2); the Faraday–Lenz law for time-invariant sources (Eq. 5.3) and the quasistatic form of Ampère's law (Eq. 5.4). These equations form the basis for describing the electromagnetic behaviour of the system under the defined assumptions and will be adapted in the subsequent derivation to model both the reduction in levitation force and the generation of drag force.

The equations are the following:

$$\bar{J} = \sigma(\bar{E} + \bar{\nu} \times \bar{B}) \tag{5.2}$$

$$\bar{\nabla} \times \bar{E} = 0 \tag{5.3}$$

$$\bar{J} = \bar{\nabla} \times \frac{\bar{B}}{\mu} \tag{5.4}$$

Eq. 5.3 is applicable to this problem because the induced currents are generated by the motion of the conductor in a static magnetic field, rather than by time-varying sources.

Assuming that the magnetic flux density has only the y component and neglecting the fringing fluxes in the z direction, the problem can be treated as 2D in the xz plane.

Accordingly, the magnetic flux density will be denoted as $B_y(x,z)$. For simplicity, the vector notation will be omitted, and this component will be referred to simply as B, with the understanding that it always points in the y direction. Ampère's law must be integrated to find the relations between the magnetic flux density and the currents. By doing so, two integration paths can be defined: the first one on the xy plane and the second one on the zy plane. Both of them are shown in Fig. 5.2. By integrating Ampère's law along these paths and assuming that the iron has infinite relative magnetic permeability, the following expressions are obtained:

$$\frac{\partial B}{\partial x} = \frac{\mu_0 b}{2\delta} J_z \tag{5.5}$$

$$\frac{\partial B}{\partial z} = -\frac{\mu_0 b}{2\delta} J_x \tag{5.6}$$

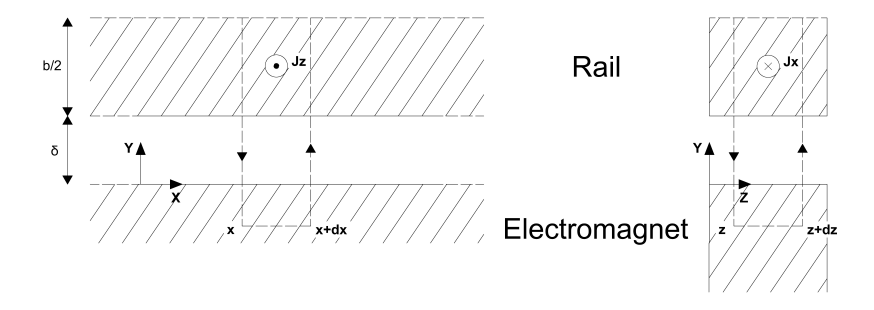


Figure 5.2: Integration paths for Ampère's law. Left: xy-plane. Right: zy-plane

5.2.2 Derivation of the total air gap flux density

Convection-diffusion partial differential equation

By combining the generalized Ohm's law (5.2), Faraday's law (5.3), and Ampère's law (5.4), the governing equation for the magnetic flux density distribution in the air gap can be derived. Applying the curl operator to both sides of Eq.(5.2) and substituting Eq. (5.3) gives:

$$\bar{\nabla} \times \bar{J} = \sigma \, \bar{\nabla} \times (\bar{\nu} \times \bar{B}) \tag{5.7}$$

Here, the right-hand side represents the curl of the motional current term. Under the uniformity assumption $\frac{\partial B}{\partial y} = 0$, the *y*-component of Eq.(5.7) becomes:

$$\left(-\frac{\partial J_z}{\partial x} + \frac{\partial J_x}{\partial z}\right)\hat{\mathbf{e}}_y = \left(\sigma v \frac{\partial B}{\partial x}\right)\hat{\mathbf{e}}_y \tag{5.8}$$

This relates the spatial variation of current density to the magnetic field gradient along x. Substituting the relations from Ampère's law (5.5) and (5.6) into Eq.(5.8) yields:

$$\frac{\partial^2 B}{\partial x^2} + \frac{\partial^2 B}{\partial z^2} - k \frac{\partial B}{\partial x} = 0 \tag{5.9}$$

where:

$$k = \frac{\mu_0 \sigma b v}{2\delta}$$

with μ_0 the permeability of free space, σ the rail's conductivity, b the pole shoe width, v the electromagnet velocity, and δ the air-gap length.

Equation (5.9) is a steady-state convection-diffusion PDE:

The first two terms represent magnetic field diffusion in *x* and *z*, while the third term models the convective transport of the field caused by motion.

Principle of superposition

Under the assumption of linear material behavior, the principle of superposition applies. The total magnetic flux density *B* in the air gap can be expressed as the sum of:

- B_e: the flux density produced directly by the excitation current in the electromagnet's coil,
- *B_i*: the flux density generated by eddy currents induced in the rail.

This gives:

$$B = B_e + B_i \tag{5.10}$$

Here, B_i represents the perturbation of the original excitation field due to motion-induced currents. Substituting Eq.(5.10) into Eq.(5.9) and separating the two contributions gives:

$$\frac{\partial^2 B_i}{\partial x^2} + \frac{\partial^2 B_i}{\partial z^2} - k \frac{\partial B_i}{\partial x} = -\frac{\partial^2 B_e}{\partial x^2} - \frac{\partial^2 B_e}{\partial z^2} + k \frac{\partial B_e}{\partial x}$$
 (5.11)

The left-hand side describes the intrinsic behavior of the induced field B_i .

The right-hand side acts as a forcing term coming from the excitation field B_e .

For tractability, we assume B_e is constant within the air gap and not influenced by fringing. It can therefore be modeled as the product of step functions:

$$B_e = B_0 \left[u(x) - u(x - l) \right] \left[u \left(z + \frac{w}{2} \right) - u \left(z - \frac{w}{2} \right) \right]$$
 (5.12)

where:

- B_0 is the uniform magnitude of the excitation field,
- $u(\cdot)$ is the Heaviside step function,
- *l* is the electromagnet length,
- w is the tooth width.

This representation treats the excitation field as uniform inside the pole area and zero outside. It greatly simplifies subsequent analytical manipulation, while still preserving the essential spatial localization of B_e .

Separation of variables

To solve the homogeneous form of Eq.(5.11), we neglect the forcing term and focus on B_i alone:

$$\frac{\partial^2 B_i}{\partial x^2} + \frac{\partial^2 B_i}{\partial z^2} - k \frac{\partial B_i}{\partial x} = 0 \tag{5.13}$$

Here, B_i is the field perturbation due solely to eddy currents in the rail.

The method of separation of variables is applicable because the PDE contains derivatives in *x* and *z* that can be decoupled.

We seek a solution of the form:

$$B(x,z) = X(x)Z(z)$$
(5.14)

where X(x) captures the variation along the motion direction, and Z(z) describes the variation along the pole width.

Substituting Eq.(5.14) into Eq.(5.13) yields:

$$Z(z)\frac{\partial^2 X(x)}{\partial x^2} + X(x)\frac{\partial^2 Z(z)}{\partial z^2} - kZ(z)\frac{\partial X(x)}{\partial x} = 0$$
(5.15)

$$\frac{1}{X(x)} \frac{\partial^2 X(x)}{\partial x^2} + \frac{1}{Z(z)} \frac{\partial^2 Z(z)}{\partial z^2} - \frac{k}{X(x)} \frac{\partial X(x)}{\partial x} = 0$$
 (5.16)

Since the first term depends only on x and the second only on z, each must equal a separation constant.

We denote it λ_n^2 , leading to:

$$-\lambda_n^2 = \frac{1}{Z(z)} \frac{\partial^2 Z(z)}{\partial z^2} \tag{5.17}$$

$$\lambda_n^2 = \frac{1}{X(x)} \frac{\partial^2 X(x)}{\partial x^2} - \frac{k}{X(x)} \frac{\partial X(x)}{\partial x}$$
 (5.18)

Equation (5.17) is a standard harmonic equation in z, with general solution:

$$Z(z) = \cos(\lambda_n z + \phi) \tag{5.19}$$

Applying the boundary conditions $B_i\left(z=\pm\frac{w}{2}\right)=0$ yields:

$$\phi = 0 \tag{5.20}$$

$$\lambda_n = (2n - 1)\frac{\pi}{w} \tag{5.21}$$

Thus, the induced field takes the form:

$$B_i(x, z) = X_n(x)\cos(\lambda_n z) \tag{5.22}$$

where each harmonic n corresponds to a spatial mode of the eddy-current-induced perturbation. The z-dependence is fully determined by the geometry, while the unknown $X_n(x)$ must be found from the x-direction PDE, incorporating the forcing term from the excitation field in Eq.(5.11).

Fourier series

The right-hand side of Eq.(5.11) involves the spatial variation of the excitation field B_e .

To handle this mathematically, we expand the z-dependence of B_e in a cosine Fourier series, which naturally matches the boundary conditions along the pole width.

Since the electromagnet moves along the x-direction, we can neglect the second derivative with respect to z in the forcing term:

$$\frac{\partial^2 B_e}{\partial z^2} \approx 0 \tag{5.23}$$

This simplification follows from the fact that the motion does not alter the spatial profile along z. From Eq.(5.12), the z-profile of B_e is given by:

$$u\left(z+\frac{w}{2}\right)-u\left(z-\frac{w}{2}\right)$$

This rectangular function (equal to 1 inside the pole width, 0 outside) can be expressed as a cosine Fourier series:

$$u\left(z + \frac{w}{2}\right) - u\left(z - \frac{w}{2}\right) = \sum_{n=1}^{\infty} C_n \cos(\lambda_n z)$$
 (5.24)

where λ_n is given by Eq.(5.21), and the Fourier coefficients C_n are:

$$C_n = \frac{4}{w} \int_0^{\frac{w}{2}} 1 \cdot \cos\left((2n - 1)\frac{\pi}{w}z\right) dz$$
 (5.25)

$$= \frac{4}{w} \cdot \frac{w}{(2n-1)\pi} \sin\left(\frac{(2n-1)\pi}{2}\right)$$
 (5.26)

$$= \frac{4}{(2n-1)\pi} \sin\left(\frac{(2n-1)\pi}{2}\right)$$
 (5.27)

Physically, these coefficients represent the amplitude of each spatial harmonic in the z-direction. Taking the derivatives of B_e with respect to x and substituting into the forcing term on the right-hand side of Eq.(5.11) gives:

$$f(x,z) = B_0 \left[-\frac{\partial}{\partial x} \left(\delta(x) - \delta(x-l) \right) + k \left(\delta(x) - \delta(x-l) \right) \right] \cdot \sum_{n=1}^{\infty} C_n \cos(\lambda_n z)$$
 (5.28)

Here, $\delta(x)$ is the Dirac delta function, arising from the derivative of the step function. Physically, these δ -terms represent the abrupt spatial discontinuity of the excitation field at the pole edges. Using the orthogonality property of cosine functions in z, we can isolate each harmonic n and obtain:

$$\frac{\partial^2 X_n(x)}{\partial x^2} - \lambda_n^2 X_n(x) - k \frac{\partial X_n(x)}{\partial x} = C_n B_0 \left[-\frac{\partial}{\partial x} \left(\delta(x) - \delta(x-l) \right) + k \left(\delta(x) - \delta(x-l) \right) \right]$$
 (5.29)

This is now a 1D non-homogeneous ODE for $X_n(x)$, where:

- The left-hand side describes the spatial decay and convection of each harmonic due to eddy currents.
- The right-hand side represents sharp source terms located at the pole's leading and trailing edges.

Fourier transform

Equation (5.29) is a non-homogeneous ODE in x for each spatial harmonic n.

A natural way to solve it is to move to the frequency domain using the Fourier transform, which converts derivatives into algebraic terms and makes the delta functions particularly easy to handle. We recall the definitions:

$$\mathscr{F}\{f(x)\} = \hat{f}(\omega) = \int_{-\infty}^{\infty} f(x) e^{-j2\pi\omega x} dx \tag{5.30}$$

$$f(x) = \frac{1}{2\pi} \int_{-\infty}^{\infty} \hat{f}(\omega) \, e^{j\omega x} d\omega \tag{5.31}$$

Here, ω is the spatial frequency in the *x*-direction.

Key Fourier transform properties needed:

$$\frac{df(x)}{dx} \longrightarrow j\omega \hat{f}(\omega)$$

$$\delta(x-l) \longrightarrow e^{j\omega l}$$
(5.32)

$$\delta(x-l) \longrightarrow e^{j\omega l} \tag{5.33}$$

These results show that derivatives become multiplication by $j\omega$, while delta functions become pure exponentials. Applying the Fourier transform to Eq.(5.29) gives:

$$-\omega^2 \hat{X}_n(\omega) - j\omega k \hat{X}_n(\omega) - \lambda_n^2 \hat{X}_n(\omega) = C_n B_0 \left[(k - j\omega) \left(1 - e^{-j\omega l} \right) \right]$$
 (5.34)

The left-hand side is now a quadratic polynomial in ω , multiplied by $\hat{X}_n(\omega)$.

The right-hand side is entirely algebraic in ω , with the factor $(1 - e^{-j\omega l})$ encoding the finite pole length.

Rearranging:

$$\hat{X}_n(\omega) = C_n B_0 \frac{(j\omega - k) \left(1 - e^{-j\omega l}\right)}{\omega^2 + i\omega k + \lambda_n^2}$$
(5.35)

Physically:

- The numerator contains $(j\omega k)$, representing the combined effect of spatial variation and convective transport.
- The denominator $\omega^2 + j\omega k + \lambda_n^2$ behaves like a damped spatial resonance, where λ_n is set by the electromagnet's width.

To return to the spatial domain, we apply the inverse transform:

$$X_n(x) = \frac{C_n B_0}{2\pi} \int_{-\infty}^{\infty} \frac{(j\omega - k) \left(e^{j\omega x} - e^{j\omega(x-l)}\right)}{\omega^2 + j\omega k + \lambda_n^2} d\omega$$
 (5.36)

The two exponentials correspond to the leading edge (x = 0) and trailing edge (x = l) contributions of the electromagnet to the induced field.

Residue theorem

To evaluate the integral in Eq.(5.36), we use the residue theorem from complex analysis. This approach is effective because the integrand is a rational function of ω multiplied by exponentials, and its poles are simple to identify.

Residue theorem

Let U be a simply connected open subset of the complex plane containing a finite set of isolated singularities $\{a_1,...,a_n\}$. If f is holomorphic in U except at these points, and γ is a positively oriented closed contour in U that does not pass through any a_k , then:

$$\oint_{\gamma} f(\omega) d\omega = 2\pi j \sum_{k=1}^{n} I(\gamma, a_k) \operatorname{Res}(f, a_k)$$
(5.37)

Here $I(\gamma, a_k)$ is the winding number of γ around a_k , and Res (f, a_k) is the residue of f at a_k . For a pole of order p at $\omega = c$:

$$\operatorname{Res}(f,c) = \frac{1}{(p-1)!} \lim_{\omega \to c} \frac{d^{p-1}}{d\omega^{p-1}} \left[(\omega - c)^p f(\omega) \right]$$
 (5.38)

Poles of the integrand

The denominator of Eq.(5.36) gives:

$$\omega^2 + j\omega k + \lambda_n^2 = 0 \tag{5.39}$$

Solving:

$$\omega = \frac{-jk \pm \sqrt{-k^2 - 4\lambda_n^2}}{2} = \frac{j}{2} \left(-k \pm \sqrt{k^2 + 4\lambda_n^2} \right)$$
 (5.40)

This yields two purely imaginary poles:

$$\alpha_n = \frac{j}{2} \left(-k + \sqrt{k^2 + 4\lambda_n^2} \right) \quad (\operatorname{Im} \alpha_n > 0)$$

$$\beta_n = \frac{j}{2} \left(-k - \sqrt{k^2 + 4\lambda_n^2} \right) \quad (\operatorname{Im} \beta_n < 0)$$
(5.41)

$$\beta_n = \frac{j}{2} \left(-k - \sqrt{k^2 + 4\lambda_n^2} \right) \quad (\operatorname{Im} \beta_n < 0) \tag{5.42}$$

Physically, these poles represent spatial decay rates of the induced field upstream and downstream of the electromagnet's geometrical edges.

Choice of integration contour

To apply the residue theorem, we must close the contour in the upper or lower half-plane so that the exponential terms in Eq.(5.36) vanish on the semicircular arc.

For $\omega = Re^{j\theta}$:

$$e^{j\omega x} = e^{-Rx\sin\theta} \cdot e^{jRx\cos\theta} \tag{5.43}$$

Thus:

$$|e^{j\omega x}| = e^{-Rx\sin\theta}$$

and similarly:

$$|e^{j\omega(x-l)}| = e^{-R(x-l)\sin\theta}$$

The sign of x or (x-l) determines whether we should close the contour in the upper $(\sin \theta > 0)$ or lower $(\sin \theta < 0)$ half-plane, following the integration paths depicted in Fig. 5.3. From this decay condition, the correct contour choice is:

- 1. x < 0: both exponentials decay in the lower half-plane (path II).
- 2. 0 < x < l: $e^{j\omega x}$ decays in the upper half-plane (path I), $e^{j\omega(x-l)}$ decays in the lower half-plane (path II).
- 3. x > l: both exponentials decay in the upper half-plane (path I).

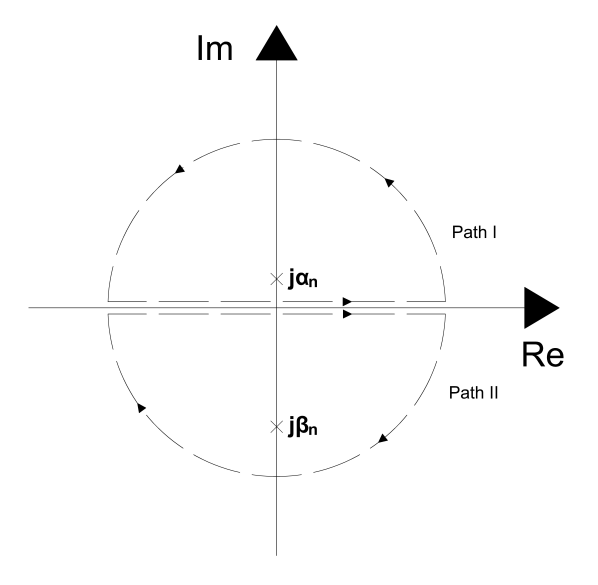


Figure 5.3: Residue theorem integration paths

Applying the residue theorem

For each x-region, we pick up the residues of the poles enclosed by the chosen contour. The results are:

1. For x < 0 (only β_n inside the contour, note the minus sign from path II orientation):

$$X_n(x) = -(2\pi j) \operatorname{Res} \left[\frac{C_n B_0(j\omega - k)(e^{j\omega x} - e^{j\omega(x-l)})}{(\omega - j\alpha_n)(\omega - j\beta_n)}, \, \omega = j\beta_n \right]$$
(5.44)

$$=C_n B_0 \frac{\alpha_n}{\alpha_n - \beta_n} \left[e^{-\beta_n x} - e^{-\beta_n (x-l)} \right]$$
(5.45)

2. For 0 < x < l (pick α_n from the first term, β_n from the second term):

$$X_n(x) = C_n B_0 \frac{1}{\alpha_n - \beta_n} \left[\beta_n e^{-\alpha_n x} - \alpha_n e^{-\beta_n (x - l)} \right]$$
 (5.46)

3. For x > l (only α_n inside the contour):

$$X_n(x) = C_n B_0 \frac{\beta_n}{\alpha_n - \beta_n} \left[e^{-\alpha_n x} - e^{-\alpha_n (x-l)} \right]$$
 (5.47)

Each expression reflects the exponential decay of the induced field away from the electromagnet edges, with different decay constants upstream and downstream.

Magnetic flux density

The total magnetic flux density in the air gap is the sum of the field produced by the excitation current B_e and that induced by eddy currents B_i (Eq.(5.10)):

$$B(x,z) = B_e(x,z) + B_i(x,z)$$

From the previous derivation, the induced component is expressed as:

$$B_i(x, z) = X_n(x)\cos(\lambda_n z)$$

while the excitation field, under the uniform-field and sharp-edge approximation, is:

$$B_e(x, z) = B_0 [u(x) - u(x - l)] \left[u \left(z + \frac{w}{2} \right) - u \left(z - \frac{w}{2} \right) \right]$$

where B_0 is the nominal flux density in the gap, u is the Heaviside step function, l is the pole length, and w is the tooth width.

Substituting $X_n(x)$ from the results of Section 5.2.6 into the above gives:

1. Inside the electromagnet (0 < x < l):

$$B(x,z) = B_0 + \sum_{n=1}^{\infty} X_n(x) \cos(\lambda_n z)$$
 (5.48)

The constant term B_0 represents the undisturbed uniform field, while the summation captures spatial harmonics due to eddy-current distortion.

2. Outside the electromagnet (x < 0 or x > l):

$$B(x,z) = \sum_{n=1}^{\infty} X_n(x) \cos(\lambda_n z)$$
 (5.49)

Here, only the induced field remains, decaying exponentially away from the electromagnet edges according to α_n and β_n .

Within the pole, B_e dominates, with B_i acting as a perturbation that reduces the net levitation force. Outside the pole, the induced field alone persists, representing the leakage of magnetic energy into the rail due to motion. The harmonic terms $\cos(\lambda_n z)$ arise from the finite electromagnet's width, with higher n corresponding to finer spatial variations in z.

5.2.3 Levitation force calculation

The levitation force is obtained from Maxwell's stress tensor, which expresses the mechanical force on a surface in terms of the magnetic field. Under the assumption that the magnetic flux density has only a *y*-component (B_y) in the gap, the relevant stress component simplifies to:

$$\sigma_{xx} = \frac{B_y^2}{\mu_0}$$

where μ_0 is the permeability of free space.

Integrating σ_{xx} over the gap surface gives the net upward force:

$$F = \frac{1}{\mu_0} \int_{-\infty}^{\infty} \int_{-\frac{w}{2}}^{\frac{w}{2}} [B(x, z)]^2 dz dx$$
 (5.50)

Substitution of B(x, z)

Replacing B(x, z) with the expressions derived previously, and performing the z-integration first, the orthogonality of the cosine terms ensures that only terms of equal harmonic order contribute to

the result. This significantly simplifies the double integral.

After carrying out the algebra and normalizing by the static (zero-speed) force:

$$F_0 = \frac{wlB_0^2}{\mu_0} \tag{5.51}$$

we obtain the dynamic levitation force:

$$F_{l} = F_{0} \sum_{n=1}^{\infty} \frac{C_{n}^{2}}{2l} \left[l + \frac{\hat{\beta}_{n}}{\alpha_{n}} (2 + \hat{\beta}_{n}) (1 - e^{-\alpha_{n}l}) + \frac{\hat{\alpha}_{n}}{\beta_{n}} (2 - \hat{\alpha}_{n}) (1 - e^{\beta_{n}l}) + \frac{2\hat{\alpha}_{n}\hat{\beta}_{n}}{\alpha_{n} + \beta_{n}} (e^{-\alpha_{n}l} - e^{\beta_{n}l}) \right]$$
(5.52)

where:

$$\hat{\alpha}_n = \frac{\alpha_n}{\alpha_n - \beta_n}, \quad \hat{\beta}_n = \frac{\beta_n}{\alpha_n - \beta_n}$$

and α_n , β_n are the spatial attenuation constants for harmonic n.

Physical interpretation

- The ratio F_1/F_0 quantifies the loss of lift due to motion.
- The exponential factors $e^{-\alpha_n l}$ and $e^{\beta_n l}$ describe how the field decays from the leading and trailing edges of the pole, respectively.
- Higher-order harmonics (n > 1) typically contribute less because C_n decreases with n, but they become more significant if the tooth width w is small compared to the gap.

5.2.4 Drag force calculation

The drag force is derived from the Lorentz force density, which represents the electromagnetic force per unit volume acting on charges and currents:

$$\vec{f} = q\vec{E} + \vec{J} \times \vec{B}$$

where \bar{E} is the electric field, \bar{B} the magnetic flux density, \bar{J} the current density, and q the charge density.

Neglecting the electric term

Under the model assumptions, the contribution from the electric field is negligible compared to the magnetic term. Thus:

$$\vec{f} \approx \vec{J} \times \vec{B}$$

From Eq.(5.5), the *z*-component of the current density can be written as:

$$J_z = \frac{2\delta}{\mu_0 b} \frac{\partial B}{\partial x}$$

and using Eq. (5.10) ($B = B_e + B_i$), the *x*-component of the Lorentz force density becomes:

$$f_x = J_z B_y = \frac{2\delta}{\mu_0 b} (B_e + B_i) \frac{\partial B_i}{\partial x}$$
 (5.53)

Volume integration

The total drag force is obtained by integrating f_x over the entire rail volume interacting with the field:

$$F_b = \frac{2\delta}{\mu_0 b} \int_{-\infty}^{\infty} dx \int_0^b dy \int_{-\frac{w}{2}}^{\frac{w}{2}} (B_e + B_i) \frac{\partial B_i}{\partial x} dz$$
 (5.54)

The *y*-integration simply yields a factor b, canceling the 1/b in front, so that:

$$F_b = \frac{2\delta}{\mu_0} \int_0^l dx \int_{-\frac{w}{2}}^{\frac{w}{2}} (B_0 + B_i) \frac{\partial B_i}{\partial x} dz$$
 (5.55)

Integration by parts

Using the identity:

$$\int (B_0 + B_i) \frac{\partial B_i}{\partial x} dx = B_0 B_i \Big|_{x=0}^{x=l} + \frac{1}{2} B_i^2 \Big|_{x=0}^{x=l}$$

and performing the z-integration, we obtain:

$$F_{b} = F_{0} \frac{\delta}{l} \sum_{n=1}^{\infty} \left\{ C_{n}^{2} \left[\hat{\alpha}_{n} \left(e^{\beta_{n} l} - 1 \right) + \hat{\beta}_{n} \left(e^{-\alpha_{n} l} - 1 \right) + \frac{1}{2} \left(\hat{\beta}_{n} e^{-\alpha_{n} l} - \hat{\alpha}_{n} \right)^{2} - \frac{1}{2} \left(\hat{\beta}_{n} - \hat{\alpha}_{n} e^{-\beta_{n} l} \right)^{2} \right] \right\}$$
 (5.56)

where F_0 is the static lift force defined in Eq. (5.51).

Physical interpretation

- The drag force F_b increases with velocity because k (in α_n and β_n) is proportional to ν .
- The first two terms inside the brackets account for interaction effects between the excitation and induced fields.
- The quadratic terms correspond to contributions from the leading and trailing edges of the pole.

5.3 Concluding remarks

In this chapter, an analytical model was formulated to predict two key phenomena in an electromagnet operating under dynamic conditions: the reduction in levitation force due to eddy current shielding in the rail and the generation of a drag force opposing motion, arising from the interaction between induced and excitation fields.

The derivation began with fundamental electromagnetic relations: Ohm's law with motional induction, Faraday's law for time-invariant sources, and the quasistatic Ampère's law. Progressively incorporated simplifying hypotheses allow for a tractable analytical formulation. Using the principle of superposition, Fourier series expansion, and Fourier transform methods combined with the residue theorem, closed-form expressions for the levitation and drag forces were obtained [Eqs. (5.52) and (5.56)].

The key outcomes of the model are:

- The model explicitly links force behavior to the geometrical parameters (l, w, δ) and rail/electromagnet material properties (σ, μ_r) , as well as to the operating velocity v.
- Higher velocities reduce the effective penetration of the magnetic field into the rail (skin effect), decreasing lift and increasing drag.
- The analytical solution separates the contributions of individual spatial harmonics, making it suitable for parametric studies.

This analytical formulation, however, is not intended to replace finite element simulations in the final design stages. Instead, its main strengths lie in:

- 1. Rapid preliminary evaluation of design trade-offs without the computational cost of FEM.
- 2. Use as a core model within optimization loops or control algorithms, where repeated evaluations are required.
- 3. Providing physical insight into the interplay between geometry, velocity, and force performance.

The limitations lie in the model's applicability, bounded by its simplifying assumptions: notably linear material behavior, uniform flux distribution across the gap width, and neglect of fringing effects in z. These must be kept in mind when interpreting results.

In the following chapters, the accuracy of this analytical model will be systematically assessed through comparison with high-fidelity FEM simulations. Both qualitative curve-shape agreement and quantitative error metrics will be used. Upon successful validation, the model can be confidently integrated into the design workflow for electromagnetic levitation systems.

Chapter 6

2D and 3D simulations in dynamic conditions

Dynamic simulations are essential for validating both the levitation and the electromagnetic drag forces under realistic operating conditions. As discussed previously, the relative motion of the electromagnet with respect to the rail induces eddy currents in the latter. These currents generate a secondary magnetic field that tends to reduce the levitation force and increase the drag force, thus leading to higher losses compared to the static case.

Two different modeling approaches were investigated in COMSOL:

- 1. The **Lorentz Term** domain, which applies the Lorentz force equation directly to the rail. This approach internally accounts for the relative motion and is able to compute only the steady-state solution.
- 2. The **Moving Mesh** feature, in which the displacement is externally prescribed by imposing a motion on the rail (equivalent to moving the electromagnet instead). In contrast to the Lorentz Term, this approach can capture both transient and steady-state behavior.

The steady-state results obtained from both modeling approaches were compared to verify consistency. It is important to note that, because motion is relative, applying a displacement to the rail is equivalent to applying it to the electromagnet.

Two orientations of the electromagnet relative to the direction of motion were considered: parallel and perpendicular, as illustrated in Fig. 6.1. While both orientations yield the same levitation force under static conditions (for identical yoke cross-section, current density, and length), their behavior under dynamic conditions differs significantly.

The perpendicular orientation has been widely studied in the Hyperloop linear motor literature (see Cho et al. [19], Jaewon et al. [20]). However, this configuration produces stronger induced

currents because the magnetic field alternates continuously between north and south poles along the direction of motion. According to Faraday's law, this variation induces significant eddy currents, which reduce levitation and increase drag.

In contrast, the parallel orientation introduces smaller variations in the magnetic field along the displacement direction, thereby reducing induced currents. Consequently, it offers lower drag forces and higher effective levitation. This orientation has been successfully adopted in recent works (e.g., Wang et al. [21], Ding et al. [22]).

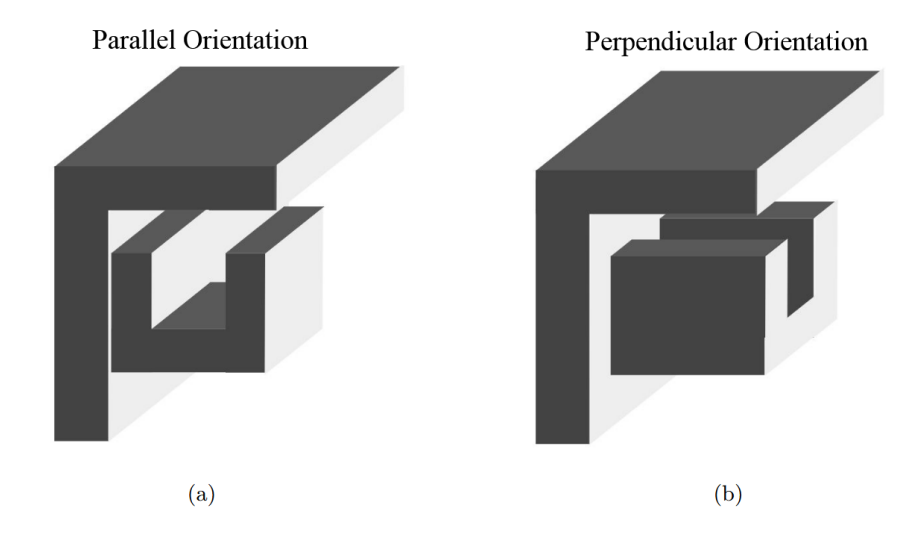


Figure 6.1: Electromagnet orientations with respect to the direction of motion: parallel and perpendicular

Another practical advantage of the parallel orientation lies in its scalability: the levitation force can be increased simply by extending the electromagnet length, without altering slot width or magnetic field distribution. In contrast, enhancing the levitation force in the perpendicular orientation requires either:

- 1. Increasing the number of adjacent coils, or
- 2. Increasing the tooth and slot width.

Both strategies introduce drawbacks. The first increases eddy currents and drag due to pole alternation, while the second increases leakage flux, reducing the levitation force.

For these reasons, only the parallel configuration was tested in 3D simulations. This choice is also motivated by a limitation of the 2D solver: in the parallel configuration, the direction of motion is orthogonal to the yoke's cross-section, preventing an accurate 2D representation of the physical behavior. Hence, 3D simulations are required to capture the correct spatial distribution of magnetic fields and induced currents.

6.1 Definition of the problem

The simulation environments must be configured differently depending on the chosen approach: one based on the **Lorentz Term** domain and the other on the **Moving Mesh** feature. While these two formulations share some common physical definitions, their implementations diverge due to the nature of the solvers.

For the **Lorentz Term** approach, the *Magnetic and Electric Fields* physics interface is employed. In contrast, the **Moving Mesh** implementation requires the *Rotating Machinery, Magnetic* interface. In the latter case, it is essential to define an *Assembly* in the Geometry module. This separates the electromagnet and the rail into distinct domains, enabling their relative motion—an essential condition for applying the Moving Mesh.

The domains common to both models are summarized below, while the specific features of each implementation will be detailed in the following subsections:

- Ampère's Law domain. Applied to all regions except the rail (i.e., air, coils, and yoke). Since
 the yoke does not experience time-varying magnetic flux, no eddy currents are induced.
 Furthermore, the optimization process ensured that the magnetic flux density remained
 below the saturation value.
- Rail definition. As the rail is subject to eddy currents, both magnetic saturation and the skin effect must be considered. In the *Magnetic and Electric Fields* interface, this requires selecting *Ampère's Law and Current Conservation in Solids*, along with a B–H curve as the magnetization model. In the *Rotating Machinery, Magnetic* interface, the standard *Ampère's Law* with a B–H curve is sufficient to capture saturation effects.
- Coils. The Coil feature is used in both models to represent the windings.
- **Force evaluation.** The *Force Calculation* feature is applied to the rail to compute electromagnetic forces as derived quantities.

6.1.1 Lorentz Term

Since the Lorentz Term formulation uses the *Magnetic and Electric Fields* interface, its setup differs from that of the Moving Mesh. Notably, it does not require an assembly geometry because no relative displacement between domains is explicitly introduced. This simplifies the problem and avoids the need for identity boundary pairs.

In addition to the common physics definitions outlined earlier, three extra domains and boundary conditions must be specified:

• Velocity (Lorentz Term). Applied to the rail, this domain defines the current density according

to the Lorentz equation:

$$\vec{J} = \sigma \left(\vec{E} + \vec{v} \times \vec{B} \right) \tag{6.1}$$

where σ is the electrical conductivity, \vec{E} the electric field, \vec{v} the velocity vector of the rail (relative to the electromagnet), and \vec{B} the magnetic flux density. This term accounts for the induced eddy currents within the rail. These currents produce a secondary magnetic field in the air gap, which interacts with the coil-generated field. The result is a reduction of the levitation force and the appearance of a drag force.

• Gauge Fixing for the Vector Potential \vec{A} . To ensure a unique solution, the Coulomb gauge condition is imposed:

$$\nabla \cdot \vec{A} = 0 \tag{6.2}$$

which introduces a Lagrange multiplier ψ into Ampère's law:

$$\nabla \times \left(\frac{1}{\mu} \nabla \times \vec{A}\right) = \vec{J} + \nabla \psi \tag{6.3}$$

The condition $\nabla \cdot \vec{A} = 0$ is then enforced through ψ , ensuring uniqueness of the solution. Although this increases the computational cost by approximately 30–60%, it avoids ambiguity in the vector potential. The resulting stiffness matrix contains zeros on its diagonal, but this does not cause issues with the direct solver used in this study.

• Magnetic Potential boundary condition. Applied to one side of the rail, this boundary condition improves convergence and sets a reference for the scalar potential ψ , ensuring it is uniquely defined.

6.1.2 Moving Mesh

In the Moving Mesh formulation, relative displacement between the rail and the electromagnet must be explicitly modeled. To achieve this, the geometry is defined as an **assembly**, enabling the creation of a boundary pair between the two components. This boundary allows for their relative motion.

The Moving Mesh workflow involves two sequential studies:

- 1. A **stationary study**, used to initialize the magnetic field distribution.
- 2. A subsequent **time-dependent study**, which applies the prescribed displacement and captures the transient and steady-state responses.

In addition to the common physics definitions, the Moving Mesh approach requires the following domains and boundary conditions:

- **Continuity boundary pair.** Applied at the rail–electromagnet interface, this condition ensures that both the scalar and vector magnetic potentials remain continuous across the moving boundary.
- Magnetic Flux Conservation. Applied to the two domains adjacent to the continuity boundary, this condition enforces conservation of magnetic flux between the sliding regions. It improves convergence by maintaining consistency in the magnetic field.
- **Gauge Fixing for the Vector Potential** \vec{A} **.** As in the Lorentz Term simulations, the Coulomb gauge condition is applied to ensure uniqueness of the solution. However, here it is imposed *only during the stationary study*, since including it in the time-dependent study would significantly increase the computational cost.
- **Zero Magnetic Scalar Potential.** Applied to a vertex in a region unaffected by the moving mesh, this condition fixes the reference for the magnetic scalar potential, ensuring numerical stability.

6.1.3 Materials

As in the stationary simulations, material properties play a crucial role, since they strongly affect the electromagnetic behavior and the resulting forces.

- **Yoke.** The *Soft Iron* material from the COMSOL library was used, with electrical conductivity set to zero. This reflects the laminated structure of the yoke, which suppresses eddy currents. Given that the optimization ensured magnetic flux densities below the saturation limit, the yoke operates far from saturation and can be treated as linear.
- **Coils.** Copper was assigned as the winding material, due to its high electrical conductivity and correspondingly reduced Joule losses compared to aluminum.
- **Rail.** Since the rail is not laminated and is subject to significant variations of magnetic flux, the *Soft Iron with Losses* material was used, with an electrical conductivity of

$$\sigma = 3 \times 10^6 \text{ S/m}.$$

This value reflects the properties of the actual rail material employed in the test track, ensuring a realistic representation of induced current and loss mechanisms.

• Air domains. Standard Air from COMSOL was used for all surrounding regions.

6.1.4 Exploitation of symmetries

To reduce computational effort, the geometric symmetries of the electromagnet were exploited. The magnetic flux density distribution is symmetric with respect to the longitudinal axis of the electromagnet. Therefore, only half of the geometry was simulated by taking a longitudinal cross-section and applying appropriate boundary conditions.

This approach reduces the number of mesh elements and simulation time significantly, while still yielding results equivalent to those of the full geometry. The validity of this method has been confirmed in the work of Pierrejean [7]. The computed forces from the half-geometry must be multiplied by two to recover the values corresponding to the complete electromagnet.

The boundary condition that ensures symmetry is the *Perfect Magnetic Conductor* (PMC), which enforces

$$\vec{n} \times \vec{H} = 0, \tag{6.4}$$

constraining the magnetic field to be tangential at the boundary. This preserves the correct symmetry of the solution in the reduced domain.

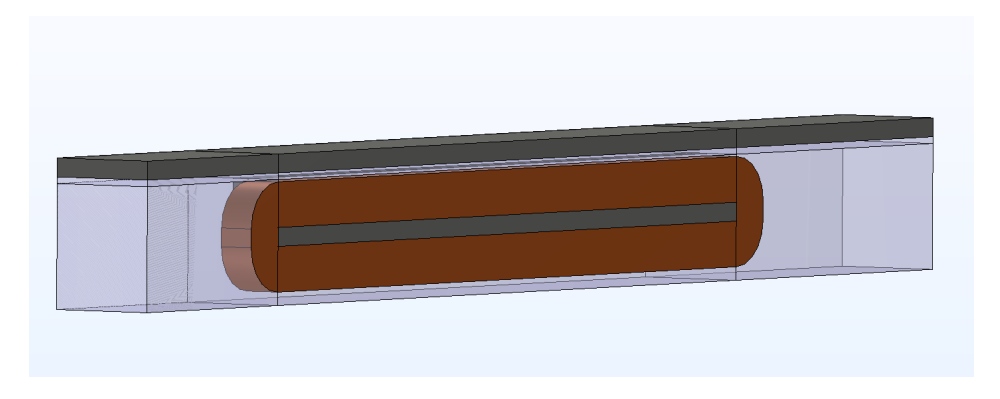


Figure 6.2: Half of the electromagnet geometry used in the simulations. The PMC boundary condition enforces the correct symmetry

6.1.5 Selection of the mesh

As in the case of steady-state simulations, mesh optimization is critical to obtain accurate results at a reasonable computational cost. However, achieving an optimal balance is more challenging in dynamic simulations because the rail experiences both magnetic saturation and the skin effect, the latter being velocity-dependent. These effects require a mesh capable of resolving sharp spatial gradients in magnetic fields and induced currents.

To address this, a dedicated mesh convergence study was performed. The refinement process focused particularly on the rail, where eddy currents concentrate near the surface. A common guideline suggests using at least three elements across the skin depth [23]. Here, a more conservative choice of ten elements was adopted to ensure higher fidelity in capturing current distributions.

The adequacy of the mesh was validated by verifying the stability of simulation results across successive refinements and by examining the spatial distribution of the relative magnetic permeability, shown in Fig. 6.3.

The final meshes used are presented in Fig. 6.4 for the Lorentz Term simulations and Fig. 6.5 for the Moving Mesh simulations. The Lorentz Term model requires a finer mesh, as it solves both magnetic and electric field equations, whereas the Moving Mesh model only solves magnetic fields but is computationally heavier due to time-dependent motion.

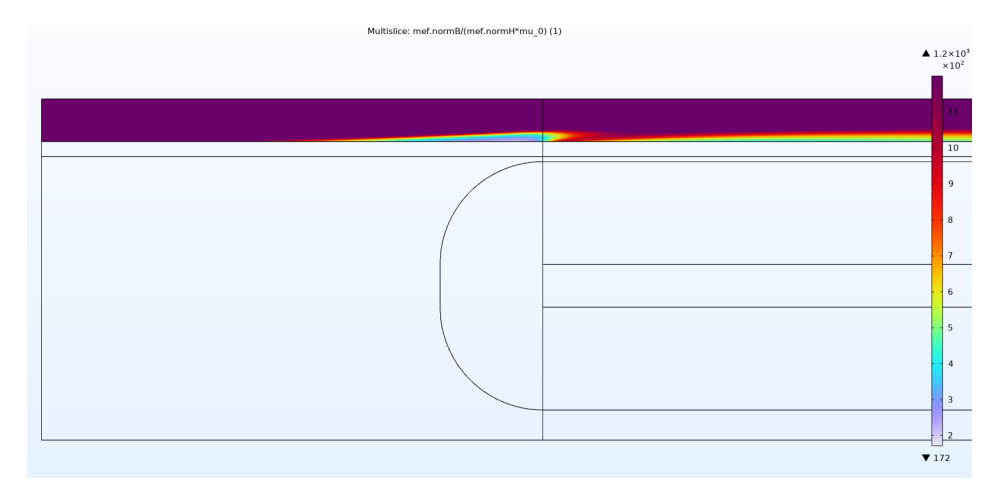


Figure 6.3: Relative magnetic permeability distribution in the rail, used to validate mesh adequacy

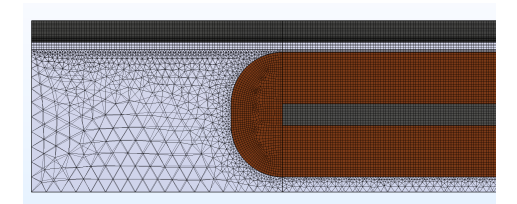


Figure 6.4: Detail of the mesh used for Lorentz Term simulations

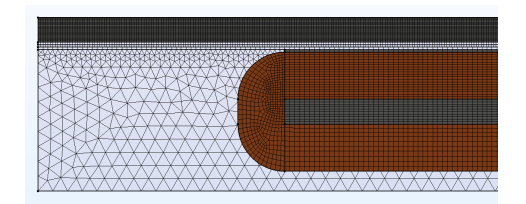


Figure 6.5: Detail of the mesh used for Moving Mesh simulations

6.2 3D simulations

As previously explained, 3D simulations are the only viable approach to model the electromagnet in the parallel orientation, since motion is orthogonal to the yoke's cross-section. In this section, the two modeling approaches, Lorentz Term and Moving Mesh, are implemented in 3D and compared with the aim of validating their consistency at steady state.

If both methods yield the same results, confidence in the simulation tools is significantly reinforced. To limit computational cost for this comparison, a reduced-size electromagnet (shorter than the optimized design) was used. Its main geometrical and electrical parameters are reported in Table 6.1.

Parameter	Value	
δ	3 [mm]	
Length	0.1 [m]	
Tooth width	9 [mm]	
Total width	50 [mm]	
Yoke height	30 [mm]	
Coil height	20 [mm]	
J	4.1 [A/mm ²]	

Table 6.1: Electromagnet parameters used for feature comparison

Both simulation setups employed a direct solver. This approach computes the inverse of the stiffness matrix explicitly, thereby avoiding the dependence on initial conditions typical of iterative solvers. For well-conditioned problems, direct solvers guarantee convergence to the correct solution. However, their computational cost grows rapidly with problem size. In this case, iterative solvers were tested but failed to converge for both configurations, which justified the use of the direct method despite its higher cost. The comparison was carried out by evaluating:

- the levitation and drag forces, which directly quantify performance, and
- the magnetic flux density distribution in the air gap, which provides physical insight into field behavior.

6.2.1 Lorentz Term

The Lorentz Term simulation was set up as described in Section 6. The stationary solver directly applies the Lorentz force formulation to model the effect of relative motion, without requiring moving geometry. Figure 6.6 shows the distribution of the magnetic flux density in a longitudinal plane cutting through the center of the electromagnet. The magnetic flux density is higher in the yoke (that has the red rectangular cross-section in Fig. 6.6) and in the rail, where the field distribution shows the presence of the edge effects generated by the presence of induced currents. This interaction reduces the levitation force and simultaneously generates the drag force.

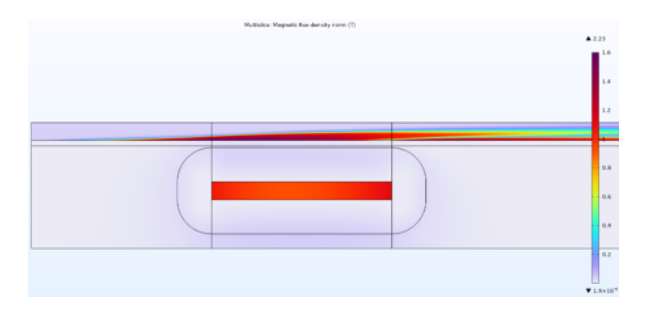


Figure 6.6: Magnetic flux density in a plane intersecting the middle of the electromagnet for the Lorentz Term simulation

6.2.2 Moving Mesh

The Moving Mesh simulation was performed according to the setup described earlier. In this formulation, relative displacement is imposed through the mesh deformation, requiring both a stationary pre-study (to initialize the field distribution) and a subsequent time-dependent study. Figure 6.7 shows the magnetic flux density at steady state in a longitudinal plane intersecting the center of the electromagnet. The distribution closely matches that obtained with the Lorentz Term approach. This confirms that both methods reproduce the same steady-state physical behavior, although the Moving Mesh is capable of also resolving transient effects.

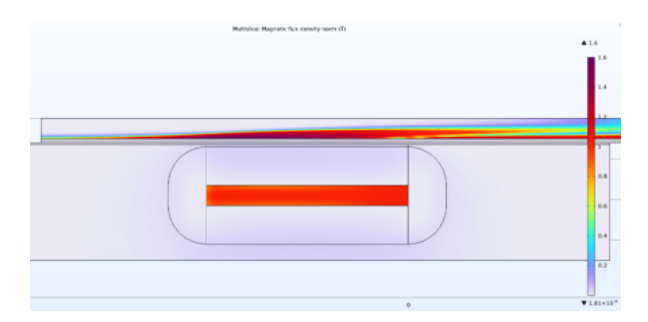


Figure 6.7: Magnetic flux density in a plane intersecting the middle of the electromagnet for the Moving Mesh simulation at steady state

6.2.3 Comparison between the Lorentz Term and Moving Mesh simulations

This subsection presents a quantitative comparison between the two methods. The levitation and drag forces were selected as the main figures of merit, since they capture the key performance aspects of the electromagnet under dynamic operation.

The simulations were carried out at a velocity of $v = 16 \,\mathrm{m/s}$, corresponding to the maximum operational speed of the pod. Figures 6.8 show the evolution of the forces over time.

As expected, the Lorentz Term yields only steady-state values, which remain constant in time. In contrast, the Moving Mesh captures the full transient behavior, starting from rest and progressively converging towards the same steady-state forces. This demonstrates that both methods are consistent, while the Moving Mesh provides additional insight into transients.

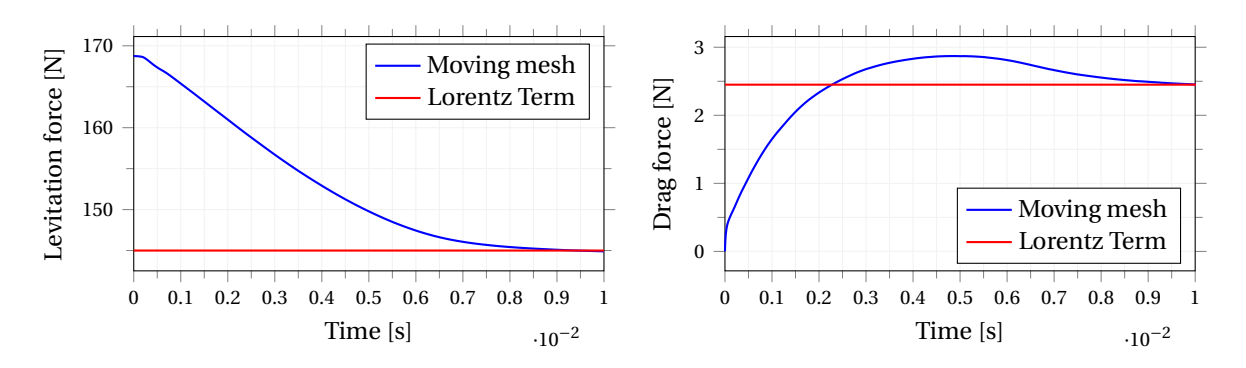


Figure 6.8: Levitation force and drag force computed with the Moving Mesh and Lorentz Term features at a velocity of $16\,\mathrm{m/s}$

Both approaches converge to identical steady-state force values, confirming their equivalence. The main difference lies in computational efficiency:

- The Lorentz Term uses a stationary solver, which computes the solution until convergence is reached.
- The Moving Mesh requires a time-dependent solver, discretizing motion and updating the fields at each step, which is much more computationally demanding.

Another interesting comparison can be conducted considering the magnetic flux densities in the air gap. In fact, from Fig. 6.9, it is clear that the two features generate the same field distribution in the air gap at steady-state. Ultimately, giving the same value of levitation and drag forces.

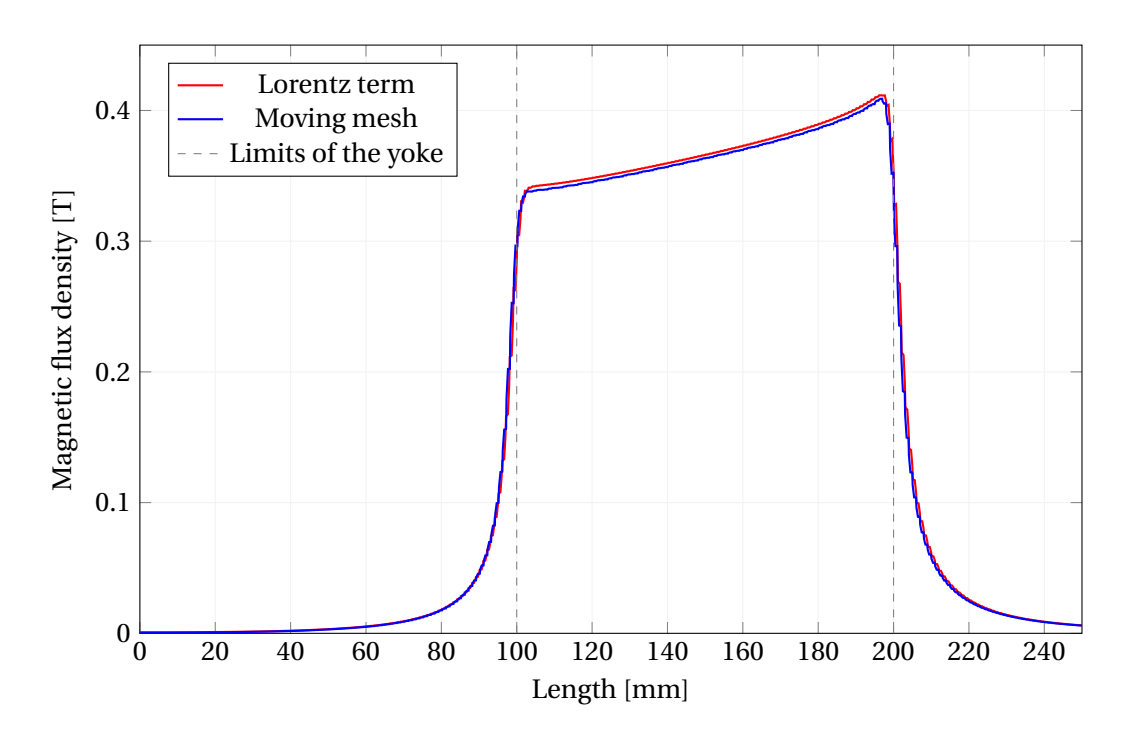


Figure 6.9: Comparison between the magnitudes of the air gap magnetic flux densities with the Moving Mesh and the Lorentz Term

As already explained, the moving mesh feature requires a time-dependent study that solves the problem at every time step. This generates higher computation times than the Lorentz Term simulations, as summarized in Table 6.2. While the Moving Mesh provides more detailed information, its cost is prohibitive when only steady-state values are required.

	Lorentz Term	Moving Mesh
Simulation time	~ 10 h	~ 1 week

Table 6.2: Computation times for the Lorentz Term and Moving Mesh simulations at $v = 16 \,\mathrm{m/s}$

Given these results, and since the focus of this study is limited to steady-state forces, the Lorentz Term method was adopted for all subsequent analyses.

6.3 Analytical model and simulations

To assess the usefulness of the analytical model as a tool for preliminary design, its predictions were compared with the simulation results. The key advantage of the analytical formulation lies in its negligible computational cost: forces can be evaluated within seconds, whereas COMSOL simulations typically require several hours or even days.

For this comparison, the Lorentz Term approach was selected, as it provides reliable steady-state results with far lower computational effort than the Moving Mesh (see Table 6.2).

Using the optimized electromagnet geometry introduced in Chapter 4, multiple dynamic simulations were performed by sweeping the velocity within the Lorentz Term domain. The levitation and drag forces obtained were normalized with respect to the stationary levitation force from COMSOL, ensuring a consistent reference point. These results were then compared with the analytical predictions given by Equations 5.52 and 5.56.

Figure 6.10 shows the outcomes of this comparison. The analytical model provides a close match to the simulated values across the tested velocity range. At the maximum velocity of $v = 16 \,\mathrm{m/s}$, the maximum error is approximately 5% for the levitation force and 15% for the drag force. Such accuracy is sufficient for preliminary design considerations, where fast evaluations are essential.

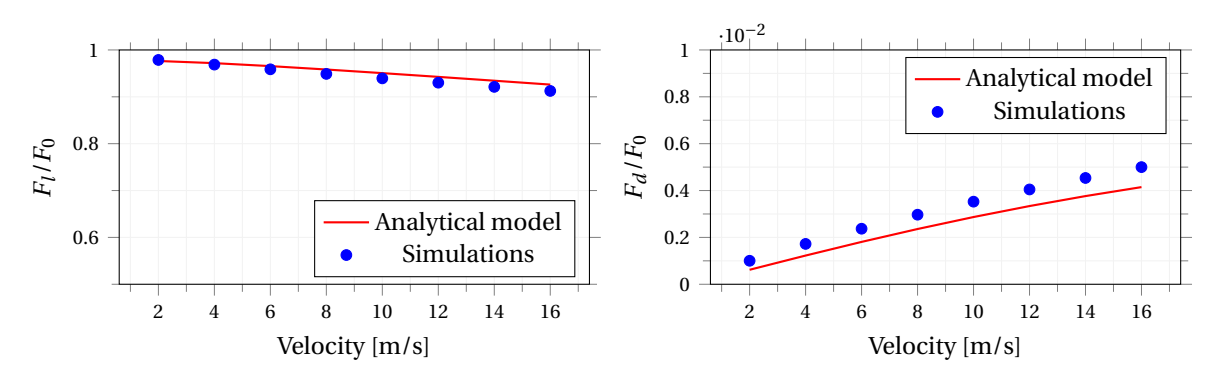


Figure 6.10: Comparison of levitation forces (left plot) and drag forces (right plot) computed with the Lorentz Term and the analytical model

In conclusion, the analytical model proves to be a powerful and reliable tool for rapid force estimation under dynamic conditions. Although full FEM simulations remain necessary for detailed validation and design refinement, the analytical approach enables efficient exploration of design options, serving as a valuable first step before more computationally intensive studies.

6.4 Real-world case study

The results of the electromagnet simulations under dynamic conditions are compared with those of the wheels at a cruising speed of 16 m/s to assess whether the electromagnets can represent an energy-efficient alternative to mechanical wheels.

The comparison focuses on the main requirements of the application: the ability to counteract the centrifugal force, the associated losses, the generated drag, and the overall weight.

For the electromagnet case, two units were considered. The total losses include both Joule losses and drag-induced losses. The forces were computed using the optimal design parameters reported in Table 4.2 and evaluated under dynamic operating conditions.

The values for the wheels were provided by the EPFLoop project group and are intended as approximate references.

Table 6.3 summarizes the comparison.

Parameter	Electromagnets	Wheels
Force	2 × 593 N	1000 N
Losses	2 × 169 W	250 W
Drag	2 × 3.25 N	10 N
Mass	2 × 6 kg	3 kg

Table 6.3: Comparison between electromagnets and wheels for pod levitation at 16m/s

From Table 6.3, it can be observed that both solutions present comparable performances for levitation. The wheels achieve the required force with slightly lower mass and reduced losses, but at the expense of higher drag. Conversely, the electromagnets exhibit lower drag and generate a comparable levitation force, though with higher overall mass and losses.

This trade-off highlights that electromagnets represent a viable alternative to mechanical wheels, especially in scenarios where reducing drag is a priority for energy efficiency at high velocities.

Furthermore, the use of electromagnets enables the possibility of achieving a fully levitating vehicle, which may be a key requirement for certain applications where mechanical contact and associated frictional losses must be eliminated. However, their higher weight and electrical losses must still be carefully considered in the overall energy balance of the system.

6.5 Concluding remarks

This chapter provided a comprehensive study of the electromagnet under dynamic conditions, with a focus on both finite element simulations and analytical validation. Two FEM approaches, the Lorentz Term and the Moving Mesh, were implemented and compared. Although both methods converged to the same steady-state results, the Lorentz Term method proved to be significantly more efficient, making it the preferred choice for steady-state analyses. Conversely, the Moving Mesh approach demonstrated its strength in capturing transient phenomena, but with a considerably higher computational cost.

The analytical model was then benchmarked against the FEM results. Despite its simplicity, it reproduced the key trends of levitation and drag forces with good accuracy (errors below 15%). Its negligible computational burden makes it particularly suited for preliminary design and parameter sweeps, where rapid insight is needed.

Overall, this chapter demonstrated the complementarity of analytical and FEM approaches: the former offers speed and intuition, while the latter ensures precision and detailed validation. This dual strategy provides a robust framework for the design and analysis of levitation electromagnets under dynamic conditions.

Chapter 7

Conclusion

The research presented in this thesis developed a complete workflow for the design, optimization, and validation of electromagnets intended for magnetic levitation applications, with a particular emphasis on the dynamic generation of electromagnetic drag and reduction in levitation force.

The first part of the work established an analytical model in stationary conditions, which was subsequently validated against FEM simulations to corroborate its accuracy. This enabled the formulation of an optimization environment, where the electromagnet geometry was tuned to maximize levitation force under given constraints.

The second part of the work extended the analysis to dynamic conditions, where both the reduction in levitation force and the generation of a drag force were evaluated. Two complementary FEM approaches, the Lorentz Term and the Moving Mesh, were compared, and the analytical model was validated against their results. The agreement between analytical predictions and FEM simulations confirmed the reliability of the simplified model, especially as a tool for rapid design iterations.

Finally, the proposed workflow was applied to a realistic case study within the EPFL Hyperloop project, where electromagnets were compared with mechanical wheels as levitation devices. The results indicated that electromagnets can be considered a competitive alternative, with comparable forces and losses, and the potential advantage of enabling a fully levitating vehicle.

Main contributions:

- Development of an optimization framework for electromagnet design under stationary conditions.
- Extension and validation of an analytical model for dynamic conditions, capturing both levitation force reduction and drag force generation.
- Comparative analysis of Lorentz Term and Moving Mesh FEM approaches, highlighting their respective advantages.
- Application of the workflow to a realistic Hyperloop prototype, demonstrating the practical

feasibility of the approach.

Future work may extend this methodology in several directions. In particular, coupling the dynamic model with control strategies could enable active regulation of levitation forces. Additionally, the analytical model in dynamic conditions can be tested with other geometries and velocities to further assess its validity.

In conclusion, this thesis contributes both methodological and practical advances to the field of magnetic levitation, providing tools that are applicable to a wide range of electromagnetic devices beyond the Hyperloop context.

Bibliography

- [1] Hannah Ritchie. "Cars, planes, trains: where do CO emissions from transport come from?" In: *Our World in Data* (2020). https://ourworldindata.org/co2-emissions-from-transport.
- [2] Mohammad Shamsuddoha, Mohammad Abul Kashem, and Tasnuba Nasir. "A Review of Transportation 5.0: Advancing Sustainable Mobility Through Intelligent Technology and Renewable Energy". In: *Future Transportation* 5.1 (2025). ISSN: 2673-7590. DOI: 10.3390/futuretransp5010008. URL: https://www.mdpi.com/2673-7590/5/1/8.
- [3] Michel Noussan, Edoardo Campisi, and Matteo Jarre. "Carbon Intensity of Passenger Transport Modes: A Review of Emission Factors, Their Variability and the Main Drivers". In: Sustainability 14.17 (2022). ISSN: 2071-1050. DOI: 10.3390/su141710652. URL: https://www.mdpi.com/2071-1050/14/17/10652.
- [4] Paul Beckert, Giacomo Pareschi, Julian Ehwald, Romain Sacchi, and Christian Bauer. "Fast as a plane, clean as a train? Prospective life cycle assessment of a hyperloop system". In: *Resources, Environment and Sustainability* 17 (2024), p. 100162. ISSN: 2666-9161. DOI: https://doi.org/10.1016/j.resenv.2024.100162.
- [5] Zhendong Liu, Sebastian Stichel, and Mats Berg. *Overview of technology and development of maglev and hyperloop systems.* TRITA-SCI-RAP 2022:001. 2022, p. 60. ISBN: 978-91-8040-125-8.
- [6] Pedro Ney Stroski. "https://www.electricalelibrary.com/en/2021/01/29/maglev-how-does-it-work/". In: *Maglev: How does it work?* 2021.
- [7] Lucien Pierrejean, Simone Rametti, André Hodder, and Mario Paolone. "A Review of Modeling, Design, and Performance Assessment of Linear Electromagnetic Motors for High-Speed Transportation Systems". In: *IEEE Transactions on Transportation Electrification* 11.1 (2025), pp. 2146–2159. DOI: 10.1109/TTE.2024.3416870.
- [8] COMSOL Multiphysics® v. 6.3. "COMSOL AB". In: www.comsol.com. Stockholm, Sweden.
- [9] A. Balakrishnan, W.T. Joines, and T.G. Wilson. "Air-gap reluctance and inductance calculations for magnetic circuits using a Schwarz-Christoffel transformation". In: *IEEE Transactions on Power Electronics* 12.4 (1997), pp. 654–663. DOI: 10.1109/63.602560.
- [10] R. Rizzo. "Magnetic circuits". In: Lectures on fundamentals of electric engineering. 2021.

- [11] Marcel Jufer. *Electromécanique*. fr. Nouv. éd., rev. et augm. Lausanne: Presses polytechniques et universitaires romandes, 1998. ISBN: 978-2-88074-285-0.
- [12] C.W.T. McLyman. *Transformer and Inductor Design Handbook, Third Edition*. Electrical Engineering and Electronics Series. Taylor Francis, 2004. ISBN: 978-0-8247-5115-9. URL: https://books.google.it/books?id=s_iMztIS8y4C.
- [13] M.K. Kazimierczuk. *High-Frequency Magnetic Components*. Wiley, 2013. ISBN: 978-1-118-71778-3. URL: https://books.google.it/books?id=oPw8AgAAQBAJ.
- [14] W.G. Hurley and W.H. Wölfle. *Transformers and Inductors for Power Electronics: Theory, Design and Applications*. EngineeringPro collection. Wiley, 2013. ISBN: 978-1-118-54467-9. URL: https://books.google.it/books?id=KAsshIYbQKoC.
- [15] Férid. KOURDA. "'Physical Modeling of Spiral Inductors Vs Air Gap for DC-DC Power Converter Design Optimization."' In: *Journal of Electrical Systems* (2018).
- [16] J. Muhlethaler, J. W. Kolar, and A. Ecklebe. "A novel approach for 3d air gap reluctance calculations". In: 8th International Conference on Power Electronics ECCE Asia. 2011, pp. 446–452. DOI: 10.1109/ICPE.2011.5944575.
- [17] Do-Kwan Hong, Ki-Chang Lee, Byung-Chul Woo, and Dae-Hyun Koo. "Optimum design of electromagnet in magnetic levitation system for contactless delivery application using response surface methodology". en. In: 2008 18th International Conference on Electrical Machines. Vilamoura, Portugal: IEEE, Sept. 2008, pp. 1–6. ISBN: 978-1-4244-1735-3. DOI: 10.1109/ICELMACH.2008.4800199. URL: http://ieeexplore.ieee.org/document/4800199/.
- [18] S. Yamamura and T. Ito. "Analysis of speed characteristics of attracting magnet for magnetic levitation of vehicles". en. In: *IEEE Transactions on Magnetics* 11.5 (Sept. 1975), pp. 1504–1507. ISSN: 0018-9464. DOI: 10.1109/TMAG.1975.1058850.
- [19] Han-Wook Cho, Chang-Hyun Kim, Jong-Min Lee, and Hyung-Suk Han. "Design and characteristic analysis of small scale magnetic levitation and propulsion system for maglev train application". en. In: 2011 International Conference on Electrical Machines and Systems. Beijing, China: IEEE, Aug. 2011, pp. 1–5. ISBN: 978-1-4577-1044-5. DOI: 10.1109/ICEMS.2011.6073910. URL: http://ieeexplore.ieee.org/document/6073910/.
- [20] Jaewon Lim, Chang-Hyun Kim, Jong-Min Lee, Hyung-suk Han, and Doh-Young Park. "Design of magnetic levitation electromagnet for High Speed Maglev train". en. In: 2013 International Conference on Electrical Machines and Systems (ICEMS). Busan: IEEE, Oct. 2013, pp. 1975–1977. ISBN: 978-1-4799-1447-0. DOI: 10.1109/ICEMS.2013.6713227. URL: http://ieeexplore.ieee.org/document/6713227/.

- [21] Linsen Wang, Qinfen Lu, and Yanxin Li. "Electromagnetic Analysis of Hybrid-Excitation Magnetic Levitation System for Low-speed Maglev Train". en. In: 2021 13th International Symposium on Linear Drives for Industry Applications (LDIA). Wuhan, China: IEEE, July 2021, pp. 1–6. ISBN: 978-1-7281-7210-1. DOI: 10.1109/LDIA49489.2021.9505963. URL: https://ieeexplore.ieee.org/document/9505963/.
- [22] Jingfang Ding, Xin Yang, Zhiqiang Long, and Ning Dang. "Three-Dimensional Numerical Analysis and Optimization of Electromagnetic Suspension System for 200 km/h Maglev Train Considering Eddy Current Effect". en. In: *IEEE Access* 6 (2018), pp. 61547–61555. ISSN: 2169-3536. DOI: 10.1109/ACCESS.2018.2876599.
- [23] Houda Zaidi, Laurent Santandrea, Guillaume Krebs, Yann Le Bihan, and Edouard Demaldent. "FEM Technique for Modeling Eddy-Current Testing of Ferromagnetic Media With Small Skin Depth". In: *IEEE Transactions on Magnetics* 50.2 (2014), pp. 129–132. DOI: 10.1109/TMAG. 2013.2283246.